The Thesis committee for Andrew Evan Mark
certifies that this is the approved version of the following thesis:

Computational modeling of stimulated emission depletion microscopy in biological cells under one- and two-photon excitation

APPROVED BY

SUPERVISING COMMITTEE:

Andrew K. Dunn, Supervisor

John A. Pearce

Computational modeling of stimulated emission depletion microscopy in biological cells under one- and two-photon excitation

by

Andrew Evan Mark, B.S.Biomed.E.

THESIS

Presented to the Faculty of the Graduate School of

The University of Texas at Austin

in Partial Fulfillment

of the Requirements

for the Degree of

MASTER OF SCIENCE IN ENGINEERING

THE UNIVERSITY OF TEXAS AT AUSTIN

December 2014

Dedicated to my family.

Acknowledgments

I would like to thank my advisor, Dr. Andrew Dunn, for his guidance and encouragement in the early stages of my graduate research. I am also grateful for the support and friendship of my lab mates. In particular, Mitchell Davis facilitated numerous discussions related to the science behind this work and provided valuable insights.

Computational modeling of stimulated emission depletion microscopy in biological cells under one- and two-photon excitation

Andrew Evan Mark, M.S.E.
The University of Texas at Austin, 2014

Supervisor: Andrew K. Dunn

The finite-difference time-domain method is used to simulate the propagation of focused beams used for stimulated emission depletion (STED) microscopy as they scatter through layers of biological cells. Depletion beams that facilitate axial and lateral confinement of the fluorescence emission are modeled, and the effective point spread function of the system as a function of focal depth is assessed under one- and two-photon excitation. Results show that the lateral depletion beam retains a well-defined minimum up to the maximum simulation depth of 42 μm. In addition, the relative spatial shift between excitation and de-excitation beam foci is less than 44 nm for all simulated depths. PSF calculations suggest that sub-diffraction imaging is possible beyond the maximum simulated depth, as long as the fluorescence emission is detectable. However, strong attenuation of the fluorescence emission by the axial confinement beam may make this beam unsuitable for sub-diffraction imaging in scattering samples.

Table of Contents

Acknowledgments **v**

Abstract **vi**

List of Tables **ix**

List of Figures **x**

Chapter 1. Introduction **1**

1.1 Fluorescence microscopy 1

1.1.1 Laser scanning microscopy 2

1.1.2 Multi-photon microscopy 3

1.1.3 Obtaining resolution beyond the diffraciton limit 5

1.1.4 The STED technique 7

Chapter 2. Focused beam formulations **11**

2.1 Excitation beam 12

2.2 De-excitation beams 15

2.2.1 Doughnut-shaped beam 16

2.2.2 Axial confinement beam 16

Chapter 3. The Finite-Difference Time-Domain Approach **20**

3.1 Governing equations 20

3.2 The FDTD algorithm 22

3.3 Boundary conditions - perfectly matched layer 27

3.4 Obtaining time-harmonic fields 28

Chapter 4. STED Microscopy Simulations **30**
4.1 Geometry and properties 30
4.2 Methods 32
4.3 Analysis 34
4.3.1 Beam scattering analysis 34
4.3.2 Point spread function analysis 35
4.4 Simulation Results 37
4.4.1 Beam scattering 37
4.4.1.1 Doughtnut-shaped de-excitation beam 37
4.4.1.2 Axial confinement de-excitation beam 39
4.4.1.3 Excitation beam 40
4.4.1.4 Beam shift quantification 40
4.4.2 Point spread function 41

Chapter 5. Conclusions **56**
5.1 Conclusions 56

Bibliography **58**

List of Tables

4.1 Cellular optical properties 46

List of Figures

2.1 Geometry used in the focused beam formulations. 13

2.2 Axial and cross-sectional profiles of the focused beams. (a-b) The circularly polarized excitation beam. (c-d) The doughnut-shaped beam. (e-f) The axial confinement beam. The axes are in units of wavelengths. 18

2.3 Volume renderings of the beam intensity distributions cut through the YZ plane. 19

3.1 The uniform Yee FDTD grid wherein each $\vec{H}$ component is surrounded by four circulating $\vec{E}$ components, and each $\vec{E}$ component is surrounded by four circulating $\vec{H}$ components. 24

4.1 Volume rendering of a typical one cell geometry with the excitation beam intensity distribution overlaid. Nuclear inhomogeneities are not shown. 31

4.2 A YZ plane projection of the three cell geometry used in the simulations. Z is the optical axis, and the colors coorespond to different refractive indices. Green arrows indicate the nominal focus locations of the beams. 33

4.3 Intensity of the central minimum for the doughnut beam as a function of nominal focus depth. Note that a focus depth of zero cooresponds to the unscattered field. 38

4.4 Lateral profiles of the doughnut de-excitation beams for varying focus depths at the effective focal plane. 47

4.5 Intensity of the central minimum for the axial confinement beam as a function of nominal focus depth. 48

4.6 Axial profiles of the axial confinement beams for varying focus depths at the effective focal plane. The z=0 location cooresponds to the nominal beam focus for a given focal depth. . . 49

4.7 Lateral profiles of the excitation beams for varying focus depths at the effective focal plane. 50

4.8 Shift in location from the nominal focus for the excitation and doughnut beams as a function of depth. 51

4.9 A demonstration of the PSF calculations in the absense of scattering for $\zeta = 3$. Row 4 - using only the lateral depletion beam. Row 5 - using both axial and lateral depletion beams at a 1:1 beam power ratio. 52

4.10 Demonstration of flouresence signal attenuation by the axial confinement beam, even in the absence of scattering. 53

4.11 Lateral PSF width as a function of focal depth for varying depletion beam powers as set by ζ. 54

4.12 Integrated lateral fluorescence signal as a function of focal depth for varying depletion beam powers. 55

Chapter 1

Introduction

STED microscopy was among the first optical microscopy techniques to surpass the resolution limit imposed by diffraction. Since its inception, the technique has been used to study a wide variety of biological samples at nanoscale spatial resolutions. Despite the resolution improvements offered by the technique, there has been little investigation of the effects of scattering on the imaging signal. To explore these effects, an electromagnetic model is used to simulate the propagation of focused laser beams used for STED as they propagate through scattering biological cells. Prior to discussing this work in detail, the fundamentals underlying the STED technique—fluorescence microscopy and methods for achieving diffraction-unlimited spatial resolution—are described.

1.1 Fluorescence microscopy

Fluorescence microscopy is widely used to study biological systems because it can provide high-resolution images and measurements related to the structure and function of biomolecules and cells. All fluorescence microscopy techniques require the use of fluorescent molecules that are typically embedded

in or attached to structures of interest in a sample. In general, the penetration depth of visible and near-infrared light, the relatively low damage potential, and the compatibility of the fluorophores with physiological imaging conditions make fluorescence microscopy the method of choice for many biological imaging applications [21].

Fluorescence occurs when a fluorophore absorbs a photon and is raised to an excited energy state, then relaxes to a lower energy state and emits a lower energy photon. For optically thin samples, widefield illumination can be used, and the resulting fluorescence emission can be imaged through an objective lens onto a detector array, directly providing an image of the sample. When imaging features within thicker samples, widefield fluorescence microscopy is less useful because the incident light will excite fluorophores throughout the sample volume, not just those residing at the focal plane. The unwanted emission light will be collected by the objective and will reduce the contrast of the signal originating from the focal plane [23]. Moreover, the degree of light scattering will increase with focal depth as the light propagates through structures of varying refractive indices, further serving to blur the image and reduce the image contrast [15].

1.1.1 Laser scanning microscopy

Laser scanning microscopy techniques have been developed that overcome the imaging depth limitations of widefield fluorescence microscopy. These techniques, including confocal microscopy and multi-photon microscopy, per-

mit three-dimensional imaging in optically thick samples [23]. In confocal microscopy, a laser beam is focused through a high numerical aperture (NA) objective in an attempt to achieve a diffraction-limited focus within the specimen. The resulting fluorescence is imaged onto a confocal pinhole placed prior to the detector in a plane conjugate to the focal plane. The pinhole prevents the detection of light that originates from planes above and below the focal plane. The beam is scanned from point to point within the specimen to generate three-dimensional images [23]. Like all microscopy techniques, confocal microscopy still suffers from increased scattering as a function of imaging depth, which prevents a true diffraction-limited focal spot from being achieved within the specimen. In addition, there is increased absorption of incident light by fluorophores in the beam path. Both of these factors limit the achievable imaging depth and resolution. Nevertheless, the achievements of confocal microscopy for 3D biological imaging in thick samples should not be underestimated. The exclusion of out-of-focus information allows for imaging of thick samples at comparable or better resolution than is achievable using widefield fluorescence microscopy in thin or sectioned samples [5].

1.1.2 Multi-photon microscopy

Multi-photon microscopy relies on multi-photon absorption to achieve inherently three-dimensional localization of fluorescence. For example, two-photon absorption is the simultaneous absorption of two lower energy photons to excite a molecule to a higher energy state. Fluorescence emission may sub-

sequently occur, just as in the linear absorption case. Two-photon absorption is a nonlinear phenomenon that depends on the square of the light intensity. The process is weak by comparison to the linear excitation process and requires very high photon densities. For microscopy, this typically requires the use of mode-locked lasers that emit pulses with a duration of 100s of femtoseconds (10^{-15}s) at very high pulse energies. The laser pulses are focused through a high NA objective, thereby creating sufficiently high photon densities for two-photon absorption near the beam focus. As a consequence, the fluorescence excitation volume is confined about the beam focus. In addition, because nearly all of the fluorescence photons are known to originate near the focus, there is no need for a confocal pinhole prior to a detector [15].

In theory, the intensity-squared dependence of two-photon absorption can result in a smaller fluorescence excitation volume than that for the confocal case at the same wavelength and depth. In practice, the wavelength used for two-photon excitation of a particular fluorophore is typically much longer (about double that of the single-photon excitation wavelength). As a consequence, the diffraction-limited focus width is larger in the two-photon case than in the confocal case. In addition, the objective lens used for two-photon imaging in thick samples is typically a lower NA water-immersion lens. The combination of these two factors results in two-photon imaging resolution that is 2 or 3 times that of confocal microscopy [6].

The most pronounced advantage of two-photon microscopy over confocal microscopy is the ability to image at depths of several hundred micrometers.

The origin of this advantage has two components: 1) The use of longer, near-infrared wavelengths results in a reduced degree of light scattering per unit depth for the excitation beam. 2) Emission photons that have scattered can still contribute to useful signal if they reach the detector [15]. For imaging in thick samples, this can increase the signal levels at depth by a factor of up to three over the confocal case [5]. Despite these advantages, the effects of scattering of the excitation beam accumulate as the imaging depth increases, effectively increasing the size of the focal volume and thereby reducing the spatial resolution. Moreover, the effect of scattering can create uncertainty in the location of the focal point and therefore the image position.

1.1.3 Obtaining resolution beyond the diffraciton limit

Diffraction effectively limits the theoretical lateral resolution of conventional far-field microscopy techniques to roughly

$$\Delta_{x,y} \approx \frac{\lambda}{2 \cdot NA} \tag{1.1}$$

and the axial resolution to

$$\Delta_z \approx \frac{2 \cdot n \cdot \lambda}{(NA)^2} \tag{1.2}$$

where λ is the free-space wavelength, n is the refractive index of the medium, and NA is the numerical aperture of the objective [3]. As an example, a high-quality immersion objective lens may have an NA of about 1.3. Assuming 400

nm incident light (nearly ultraviolet), the lateral resolution in a conventional microscope should exceed about 150 nm, and axial resolution should exceed about 620 nm in the absence of scattering and with ideal detection.

Over the past two decades, a number of microscopy techniques have been developed that overcome the resolution barrier imposed by diffraction. These techniques may generally be grouped into two categories: those based on stochastic switching of fluorophores, and those based on point spread function (PSF) engineering [14]. Techniques based on stochastic switching exploit the single-molecule nature of fluorophores to precisely locate their individual positions at a level below the diffraction limit, typically within nanometers. Precise localization is achieved by allowing only single fluorophores to emit per detectable area at any given time. The detection of a large number of single-molecule events allows for the reconstruction of the fluorophore distribution and therefore an image with resolution below the diffraction limit. There are numerous mechanisms for switching the fluorophores and ensuring that only a subpopulation of fluorophores emits per unit time. The switching mechanisms rely on the so-called RESOLFT concept, which stands for reversible saturable optical fluorescence transitions. For example, PALM (photoactivation localization microscopy) uses photoswitchable fluorescent proteins that are toggled between bright and dark states. Other techniques, such as dSTORM (direct stochastic optical reconstruction microscopy) and GSDIM (ground-state depletion with individual molecule return) use synthetic dyes that switch between bright and dark states [21].

1.1.4 The STED technique

Among techniques that rely on PSF engineering, stimulated emission depletion (STED) microscopy was one of the first RESOLFT techniques to be developed [14]. It is a far-field laser scanning microscopy technique like confocal or multi-photon microscopy. The STED technique involves exciting dye molecules in a labeled specimen using a focused, pulsed excitation beam. After the excitation pulse, the sample is usually illuminated with a red-shifted and higher power de-excitation beam that nominally has an intensity null centered about the focal point of the excitation beam [13]. The de-excitation beam induces stimulated emission in a sub-population of the excited dye molecules. Dye molecules that did not undergo stimulated emission are left to spontaneously emit fluorescence light. As the de-excitation power is increased relative to the excitation power, the dye transition is increasingly saturated, and the resulting fluorescence spot size shrinks about the excitation beam focus to a size below the diffraction limit.

The de-excitation beam is chosen to be red-shifted with respect to the excitation light so that the probability of simulated emission is substantially higher than the probability of re-excitation of the fluorophore. In addition, the delay between excitation and de-excitation pulses is typically chosen such that the the vibrational relaxation in the excited state has time to complete (typically a few ps). This puts the excited molecule in a long-lived state during which stimulated emission can effectively occur. This also explains why the STED pulse is typically much longer than the excitation pulse [22].

In a traditional STED microscope, the de-excitation beam is conditioned to form a doughnut shape with a null at roughly the center of the excitation beam focus, but with high intensity at the periphery [8]. The high intensity periphery provides lateral confinement of the fluorescence emission via stimulated emission. To enhance axial resolution, a beam with an intensity minimum that is axially confined can be generated [18]. When the axial and lateral confinement beam are combined, scanning of co-aligned excitation and de-excitation beams can yield enhancements in axial and lateral resolution over the traditional confocal microscope [32].

In theory, the STED technique is diffraction-unlimited: the power of the de-excitation beam can be increased further to saturate the transition and decrease the fluorescence spot size. In practice, the de-excitation beam power, and hence the spatial resolution, is limited by photo-destruction of the fluorophore and light scattering [10]. In addition, the fluorescence signal must be strong enough (and therefore the fluorescence spot large enough) to be detected over the leaked background light and shot noise from the photo detector.

STED microscopy has been used to visualize numerous biological structures on spatial scales that were once accessible only to electron microscopy. This includes the visualization of proteins, their structure, and even their distribution on a sub-organelle level [21]. The lateral resolution achievable using a doughnut de-excitation beam typically varies between 30 to 80 nm for biological samples depending on the properties of the samples and the de-excitation

laser power [21]. Axial resolutions in a biological sample of roughly 200 nm have been achieved using an axial confinement beam and a single objective lens [32]. The use of multiple objective lenses and STED in the isoSTED microscope has yielded isotropic resolution on the order of 30 nm and has been used to image mitochondrial membranes [25]. Despite the enhanced resolution capabilities, STED microscopy in biology has largely been limited to the study of structures in dissociated cells or cells close to tissue surfaces. To the best of my knowledge, only one study has achieved optical superresolution via single photon excitation and STED at depths greater than 100 μm (Urban et. al. 2011) [30].

It has more recently been demonstrated that two-photon excitation can be used in combination with single-photon STED to achieve optical superresolution [2, 6, 20]. This approach retains the advantages of two-photon microscopy—increased imaging depth in highly scattering samples due to reduced scattering, and also results in sub-diffraction lateral resolution. To date, this approach has achieved lateral spatial resolution that is four to five times better than that of conventional two-photon microscopy [2]. This approach appears promising for nanoscale imaging applications in highly scattering brain tissues [2].

Despite the resolution improvements offered by STED microscopy, there has been comparatively little exploration of the depth limits of the technique in scattering samples. Because STED microscopy depends on the alignment of the excitation and de-excitation beam profiles near focus, it is important

to understand how the beam profiles are perturbed with increasing imaging depth. In particular, it is useful to know whether both the excitation beam and de-excitation beams remain co-aligned after scattering, and whether the depth of the central intensity minimum of the de-excitation beam is maintained. These factors both may alter the effective PSF of the STED microscope and consequently alter the fluorescence signal strength and achievable resolution.

The goal of this research is to characterize the the propagation of beams used for STED imaging through scattering biological cells. In this pursuit, a 3D finite-difference time-domain (FDTD) electromagnetic model [7,26] is modified and used to simulate multiple biological cells defined by spatially varying refractive indices. Vector diffraction theory is used to obtain the electromagnetic fields for the excitation and de-excitation beams, and these fields are imposed as the incident fields in the model. The model computes the near field optical intensity distributions in the presence of the scattering cells. Simulations are run for the excitation beam and de-excitation beams focused to multiple depths within the sample, and a model of stimulated emission from the fluorescence state is used to compute the resultant PSF. The beam profiles, the resultant PSF, and the fluorescence signal strength are assessed as a function of focal depth for both single- and two-photon excitation STED microscopy.

Chapter 2

Focused beam formulations

In a rigorous electromagnetic model of light microscopy, it is important to take in to account the polarization state of light. Many common models of beam propagation consider the state of polarization to be unchanged by focusing, an approximation that does not in general hold true. In optical microscopy, for example, light is typically focused by a high NA objective lens that introduces substantial field components in the direction of propagation of the beam [24]. The specific polarization of light near focus is also important for determining the interaction of the incident fields with scatterers. The properties and distribution of the scatterers will affect the effective PSF of the imaging system, which essentially defines the system's practical spatial resolution. In this investigation, the beams are computed using a vectorial ray tracing approach that accounts for both geometrical and polarization effects related to focusing [33]. These fields are later used as the incident fields in light scattering models to rigorously predict the effective PSF of the STED microscope given a particular geometry of scatterers.

2.1 Excitation beam

The first beam required for the STED microscopy simulations is the fluorescence excitation beam. The excitation beam used in the simulations is a uniform plane wave that has been circularly polarized and focused through a high numerical aperture (NA) objective lens. Circular polarization is used to maximize the excitation probability of flourophores, which are assumed to be randomly oriented. To model the beam, the theoretical formulation originally posed by Richards and Wolf [33] [24] is followed and all lens aberrations are ignored. The field near the focus of the objective is described by the Debye-Wolf integral [11]:

$$\vec{E}(\rho,\varphi,z) = jC\int_0^{\theta_{max}}\int_0^{2\pi}\vec{E}_{FF}(\theta,\phi)e^{jkz\cos\theta}e^{jk\rho\sin\theta\cos(\phi-\varphi)}\sin\theta\,d\phi\,d\theta. \quad (2.1)$$

$\vec{E}_{FF}(\theta,\phi)$ is the electric field just after refraction by the lens (in the far-field), and the coordinates θ and ϕ are the azimuthal angle and polar angle, respectively. Here, θ defines the divergence angle of a conjugate ray, one that enters the lens parallel to the optical axis and passes through geometric focus after refraction. The coordinates (ρ,φ,z) designate the field point in cylindrical coordinates, where z is the distance along the optical axis from the geometric focal point. $2\theta_{max}$ is the angle that the diameter of the exit pupil subtends at the geometric focus, and C is a scaling factor that will be henceforth ignored. The geometry of the problem is depicted in Figure 2.1.

Assuming the beam is initially x-polarized before passing through a left-hand quarter waveplate to become circularly polarized, the field $\vec{E}_{FF}(\theta,\phi)$

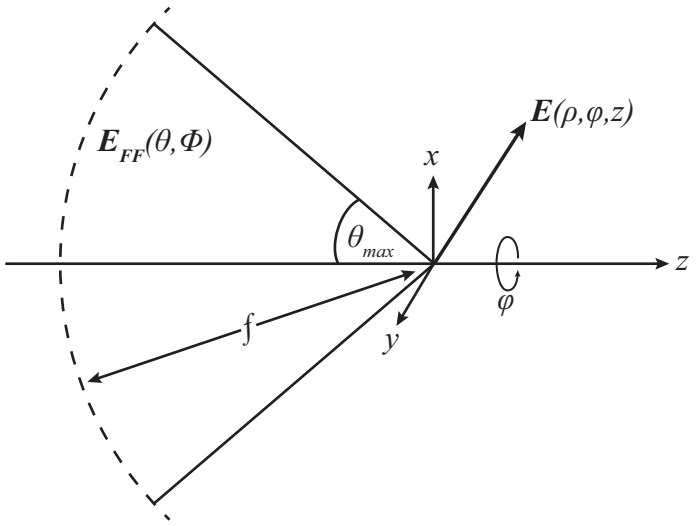

Figure 2.1: Geometry used in the focused beam formulations.

can be determined using the generalized Jones matrices [11].

$$\vec{E}_{FF}(\theta,\phi) = \sqrt{\cos\theta}\cdot\mathbf{R}^{-1}\cdot\mathbf{L}\cdot\mathbf{R}\cdot\mathbf{BS}_{\lambda/4}\cdot\vec{E}_{inc} \tag{2.2}$$

$$\mathbf{R} = \begin{pmatrix} \cos\phi & \sin\phi & 0 \\ -\sin\phi & \cos\phi & 0 \\ 0 & 0 & 1 \end{pmatrix} \tag{2.3}$$

$$\mathbf{L} = \begin{pmatrix} \cos\theta & 0 & \sin\theta \\ 0 & 1 & 0 \\ -\sin\theta & 0 & \cos\theta \end{pmatrix} \tag{2.4}$$

$$\mathbf{BS}_{\lambda/4} = \begin{pmatrix} 1 & -j & 0 \\ j & 1 & 0 \\ 0 & 0 & 1 \end{pmatrix} \tag{2.5}$$

$$\vec{E}_{inc} = \begin{pmatrix} 1 \\ 0 \\ 0 \end{pmatrix} \tag{2.6}$$

The matrices $\mathbf{R}$ and $\mathbf{L}$ transform the coordinate system to that used in the focal region. $\mathbf{BS}_{\lambda/4}$ is the generalized Jones matrix corresponding to the left-handed quarter waveplate (QWP), and $\vec{E}_{inc}$ is the Jones vector of the initially x-polarized light. The factor $\sqrt{\cos\theta}$ arises from energy conservation requirements for the fields before and after refraction by the objective [11]. After expanding Equation (2.2), the following integral identities are used to integrate Equation (2.1) analytically over ϕ for each of the Cartesian vector components:

$$\int_0^{2\pi} \cos(n\phi) e^{jx\cos(\phi-\varphi)}\, d\phi = 2\pi j^n \cos(n\varphi) J_n(x) \tag{2.7}$$

$$\int_0^{2\pi} \sin(n\phi) e^{jx\cos(\phi-\varphi)}\, d\phi = 2\pi j^n \sin(n\varphi) J_n(x) \tag{2.8}$$

Here J_n denotes the n^{th} order Bessel function of the first kind. Thus, the simplified expression for the electric field of the excitation beam near the geometric focus can be written as:

$$\vec{E}_c(\rho,\varphi,z) = \begin{pmatrix} E_{c,x} \\ E_{c,y} \\ E_{c,z} \end{pmatrix} = \begin{pmatrix} I_{c1} + I_{c2}\, e^{-j2\varphi} \\ j(I_{c1} - I_{c2}\, e^{j2\varphi}) \\ -2jI_{c3}\, e^{j\varphi} \end{pmatrix} \tag{2.9}$$

where

$$I_{c1} = \int_0^{\theta_{max}} \sqrt{\cos\theta}\sin\theta(1+\cos\theta)J_0(k\rho\sin\theta)e^{jkz\cos\theta}\,d\theta \tag{2.10}$$

$$I_{c2} = \int_0^{\theta_{max}} \sqrt{\cos\theta}\sin\theta(1-\cos\theta)J_2(k\rho\sin\theta)e^{jkz\cos\theta}\,d\theta \tag{2.11}$$

$$I_{c3} = \int_0^{\theta_{max}} \sqrt{\cos\theta}\sin^2\theta J_1(k\rho\sin\theta)e^{jkz\cos\theta}\,d\theta \tag{2.12}$$

In practice, the three integrals are evaluated numerically to compute the incident electric field a each point in the model grid.

2.2 De-excitation beams

Two different beams are used to model the de-excitation process: a doughnut-shaped beam with an intensity null along the length of optical axis, and a beam with an axially confined intensity minimum about the focal point. The doughnut-shaped beam permits simulation of traditional STED microscopy, and the incoherent superposition of the two de-excitation beams permits simulation of 3D-confined STED microscopy. To generate either de-excitation beam in practice, a particular phase retarder is inserted into the beam path prior to the objective lens. To model the general effect of the phase retarder, a spatially varying phase term $e^{j\delta(\theta,\phi)}$ multiplies the field in Equation (2.2), where $\delta(\theta,\phi)$ denotes the phase retardation function.

2.2.1 Doughnut-shaped beam

To obtain the doughnut-shaped beam, a collimated beam is passed through a vortex phase mask with a $0 - 2\pi$ helical phase ramp before passing through a QWP to be circularly polarized [18]. In this case, the phase retardation term for the phase mask is simply $e^{j\phi}$. Using the identity

$$\int_0^{2\pi} e^{jn\phi} e^{jx\cos(\phi-\varphi)}\, d\phi = 2\pi j^n e^{jn\varphi} J_n(x) \tag{2.13}$$

to integrate analytically over ϕ, Equation (2.1) can be simplified to:

$$\vec{E}_v(\rho,\varphi,z) = \begin{pmatrix} E_{v,x} \\ E_{v,y} \\ E_{v,z} \end{pmatrix} = \begin{pmatrix} I_{v1}\, e^{j\varphi} + I_{v2}\, e^{j3\varphi} \\ j(I_{v1}\, e^{j\varphi} - I_{v2}\, e^{j3\varphi}) \\ -2jI_{v3}\, e^{j2\varphi} \end{pmatrix} \tag{2.14}$$

where

$$I_{v1} = \int_0^{\theta_{max}} \sqrt{\cos\theta}\sin\theta(1+\cos\theta) J_1(k\rho\sin\theta) e^{jkz\cos\theta}\, d\theta \tag{2.15}$$

$$I_{v2} = \int_0^{\theta_{max}} \sqrt{\cos\theta}\sin\theta(1-\cos\theta) J_3(k\rho\sin\theta) e^{jkz\cos\theta}\, d\theta \tag{2.16}$$

$$I_{v3} = \int_0^{\theta_{max}} \sqrt{\cos\theta}\sin^2\theta J_3(k\rho\sin\theta) e^{jkz\cos\theta}\, d\theta. \tag{2.17}$$

2.2.2 Axial confinement beam

To obtain the second de-excitation beam with an axially-confined intensity minimum near the focal point, the vortex phase mask is replaced with a phase mask consisting of a central circular area with a π-phase retardation. In this case, the phase delay term can be written as

$$e^{j\delta(\theta,\phi)} = \begin{cases} -1 & \theta \leq \frac{\theta_{max}}{2} \\ 1 & \frac{\theta_{max}}{2} < \theta \leq \theta_{max}. \end{cases} \tag{2.18}$$

The beam can thus be expressed according to Equation (2.9), where each of the 3 integrals must now be computed over the two θ intervals. Figure 2.2 shows the resulting axial and cross-sectional intensity distributions of the excitation and de-excitation beams. Figure 2.3 portrays the same information in the form of volume renderings.

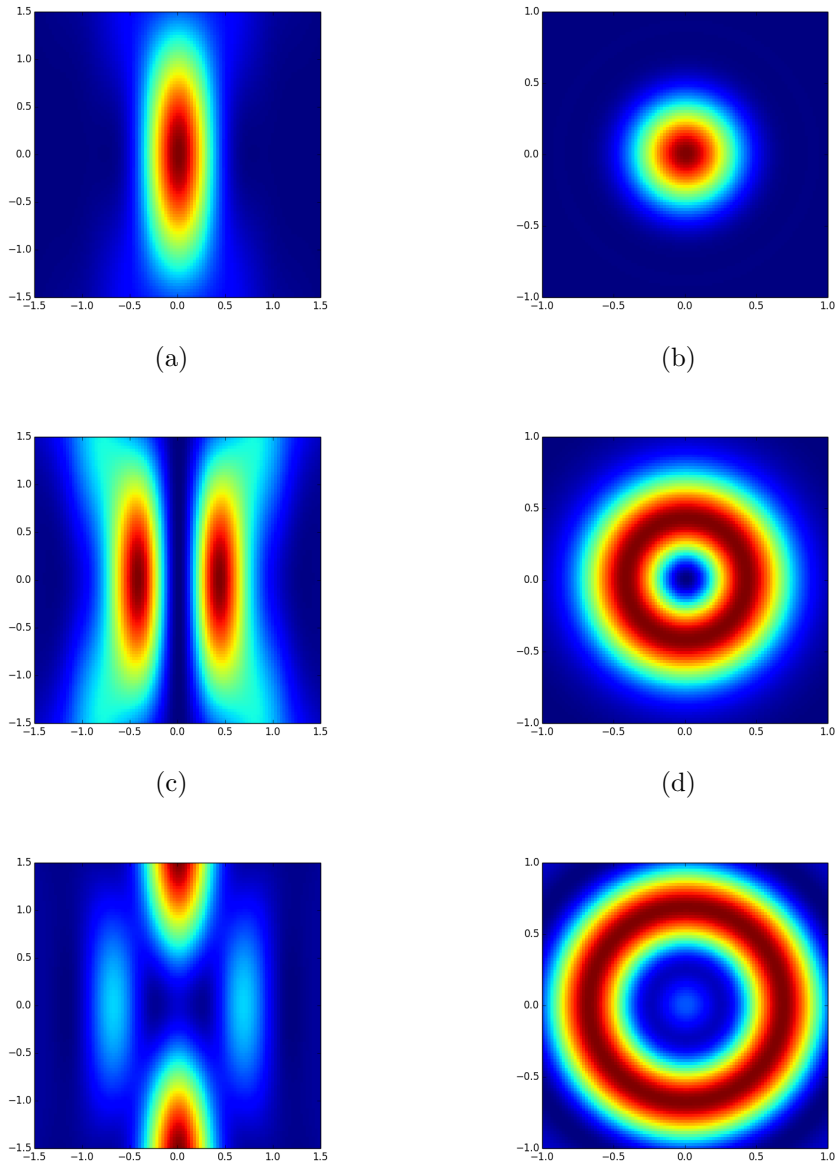

Figure 2.2: Axial and cross-sectional profiles of the focused beams. (a-b) The circularly polarized excitation beam. (c-d) The doughnut-shaped beam. (e-f) The axial confinement beam. The axes are in units of wavelengths.

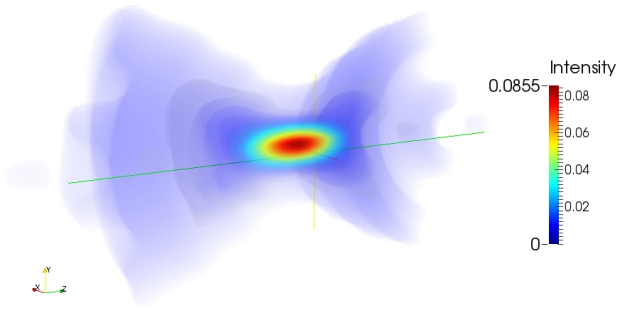

(a) Excitation beam

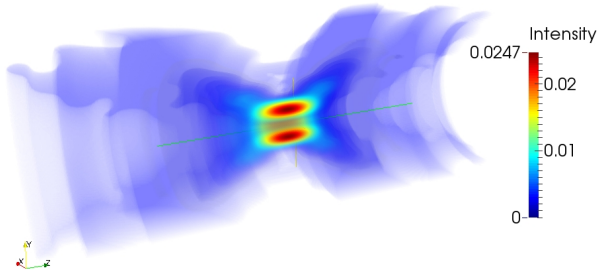

(b) Doughnut-shaped beam

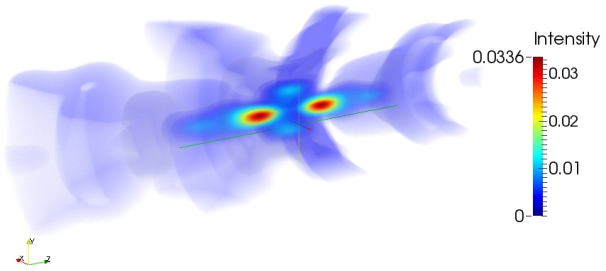

(c) Axial confinement beam

Figure 2.3: Volume renderings of the beam intensity distributions cut through the YZ plane.

Chapter 3

The Finite-Difference Time-Domain Approach

With the analytical expressions for the microscope illumination fields calculated, the next step is to calculate how light is scattered from the various structures in a sample. The finite-difference time-domain (FDTD) method, originally proposed by Yee [34], provides a three-dimensional vector computational solution to Maxwell's equations. The FDTD method directly solves Maxwell's curl equations by discretizing the electric and magnetic fields in space and time. This study uses the FDTD technique to model optical scattering from cells.

3.1 Governing equations

In a region free of current sources, Maxwell's curl equations can be written

$$\epsilon_0 \epsilon_r \frac{\partial \vec{E}}{\partial t} = \nabla \times \vec{H} - \sigma \vec{E} \tag{3.1}$$

$$\mu_0 \mu_r \frac{\partial \vec{H}}{\partial t} = -\nabla \times \vec{E} - \sigma^* \vec{H} \tag{3.2}$$

where the electric and magnetic conductivity (σ, σ^*) and the relative electric permittivity and magnetic permeability (ϵ_r, μ_r) may vary arbitrarily through-

out the model space. For focused beam simulations, it is convenient to decompose the total fields into the incident fields and the scattered fields because the analytical expressions for the incident fields are known.

$$\begin{aligned} \vec{E} &= \vec{E}_{inc} + \vec{E}_{scat} \\ \vec{H} &= \vec{H}_{inc} + \vec{H}_{scat} \end{aligned} \tag{3.3}$$

Due to the linearity of the curl equations, Equations (3.1) and (3.2) may be written for the incident field assuming the background medium is free space:

$$\epsilon_0 \frac{\partial \vec{E}_{inc}}{\partial t} = \nabla \times \vec{H}_{inc} \tag{3.4}$$

$$\mu_0 \frac{\partial \vec{H}_{inc}}{\partial t} = -\nabla \times \vec{E}_{inc} \tag{3.5}$$

By again invoking the linearity property, Equation (3.4) may be subtracted from (3.1) and Equation (3.5) from (3.2) to obtain

$$\epsilon_0 \epsilon_r \frac{\partial \vec{E}_{scat}}{\partial t} + \sigma \vec{E}_{scat} = \nabla \times \vec{H}_{scat} - \sigma \vec{E}_{inc} - \epsilon_0(\epsilon_r - 1)\frac{\partial \vec{E}_{inc}}{\partial t} \tag{3.6}$$

$$\mu_0 \mu_r \frac{\partial \vec{H}_{scat}}{\partial t} + \sigma^* \vec{H}_{scat} = -\nabla \times \vec{E}_{scat} - \sigma^* \vec{H}_{inc} - \mu_0(\mu_r - 1)\frac{\partial \vec{H}_{inc}}{\partial t}. \tag{3.7}$$

For simplicity, it is further assumed that the materials of interest, the cellular structures, organelles, and intra- and extracellular fluids, are nonconductive ($\sigma = \sigma^* = 0$) and nonmagnetic ($\mu_r = 1$) at optical frequencies. Under these conditions, Eq. (3.6) and Eq. (3.7) reduce to

$$\nabla \times \vec{H}_{scat} = \epsilon_0 \epsilon_r \frac{\partial \vec{E}_{scat}}{\partial t} + \epsilon_0(\epsilon_r - 1)\frac{\partial \vec{E}_{inc}}{\partial t} \tag{3.8}$$

$$\nabla \times \vec{E}_{scat} = -\mu_0 \frac{\partial \vec{H}_{scat}}{\partial t}. \tag{3.9}$$

Eqs. (3.8) and (3.9) are the basis of the FDTD algorithm used for the light scattering simulations. Using this formulation, the FDTD algorithm needs only to solve for the scattered fields because the incident fields are known throughout the simulation volume at each time step. Furthermore, the incident fields are not propagated through the FDTD grid, and therefore are not subject to phase errors that may accumulate due to numerical dispersion. In addition, it is only necessary to compute the incident field where there are scatterers ($\epsilon_r \neq 1$).

3.2 The FDTD algorithm

To obtain the finite-difference equations corresponding to the scattered-field form of Maxwell's curl equations, Equations (3.8) and (3.9) are expanded in terms of Cartesian components:

$$\epsilon \frac{\partial E_{scat,\,x}}{\partial t} = \frac{\partial H_{scat,\,z}}{\partial y} - \frac{\partial H_{scat,\,y}}{\partial z} - \epsilon_0(\epsilon_r - 1)\frac{\partial E_{inc,\,x}}{\partial t} \tag{3.10}$$

$$\epsilon \frac{\partial E_{scat,\,y}}{\partial t} = \frac{\partial H_{scat,\,x}}{\partial z} - \frac{\partial H_{scat,\,z}}{\partial x} - \epsilon_0(\epsilon_r - 1)\frac{\partial E_{inc,\,y}}{\partial t} \tag{3.11}$$

$$\epsilon \frac{\partial E_{scat,\,z}}{\partial t} = \frac{\partial H_{scat,\,y}}{\partial x} - \frac{\partial H_{scat,\,x}}{\partial y} - \epsilon_0(\epsilon_r - 1)\frac{\partial E_{inc,\,z}}{\partial t} \tag{3.12}$$

$$\mu_0 \frac{\partial H_{scat,\,x}}{\partial t} = \frac{\partial E_{scat,\,y}}{\partial z} - \frac{\partial E_{scat,\,z}}{\partial y} \tag{3.13}$$

$$\mu_0 \frac{\partial H_{scat,\,y}}{\partial t} = \frac{\partial E_{scat,\,z}}{\partial x} - \frac{\partial E_{scat,\,x}}{\partial z} \tag{3.14}$$

$$\mu_0 \frac{\partial H_{scat,\,z}}{\partial t} = \frac{\partial E_{scat,\,x}}{\partial y} - \frac{\partial E_{scat,\,y}}{\partial x} \tag{3.15}$$

Prior to discretizing these equations, it is necessary to introduce the model grid geometry, originally describe by Yee [34]. In the grid, the $\vec{E}$ and $\vec{H}$ components are centered in 3D space such that each $\vec{E}$ component is surrounded by four circulating $\vec{H}$ components, and each $\vec{H}$ component is surrounded by four circulating $\vec{E}$ components. This arrangement is shown in Figure 3.1. A point in the uniform grid is denoted as

$$(x, y, z) = (i\Delta, j\Delta, k\Delta) \tag{3.16}$$

where Δ is the grid spacing, x, y, and z are the spatial coordinates, and i, j, and k are integers. Furthermore, a point in time is denoted as

$$t = l\Delta t \tag{3.17}$$

where Δt denotes the time increment and l is an integer.

The spatial and temporal derivatives may be approximated using central differences:

$$\frac{\partial u|^l_{i,\,j,\,k}}{\partial x} = \frac{u|^l_{i+1/2,\,j,\,k} - u|^l_{i-1/2,\,j,\,k}}{\Delta} \tag{3.18}$$

$$\frac{\partial u|^l_{i,j,k}}{\partial t} = \frac{u|^{l+1/2}_{i,\,j,\,k} - u|^{l-1/2}_{i,\,j,\,k}}{\Delta t} \tag{3.19}$$

The $\pm 1/2$ in the i subscript of Eq. (3.18) denotes a spatial finite difference over $\pm\,\Delta/2$. This notation is used so that the $\vec{E}$ and $\vec{H}$ components are separated by $\Delta/2$, as shown in the Yee grid, Figure 3.1. Analogously, the

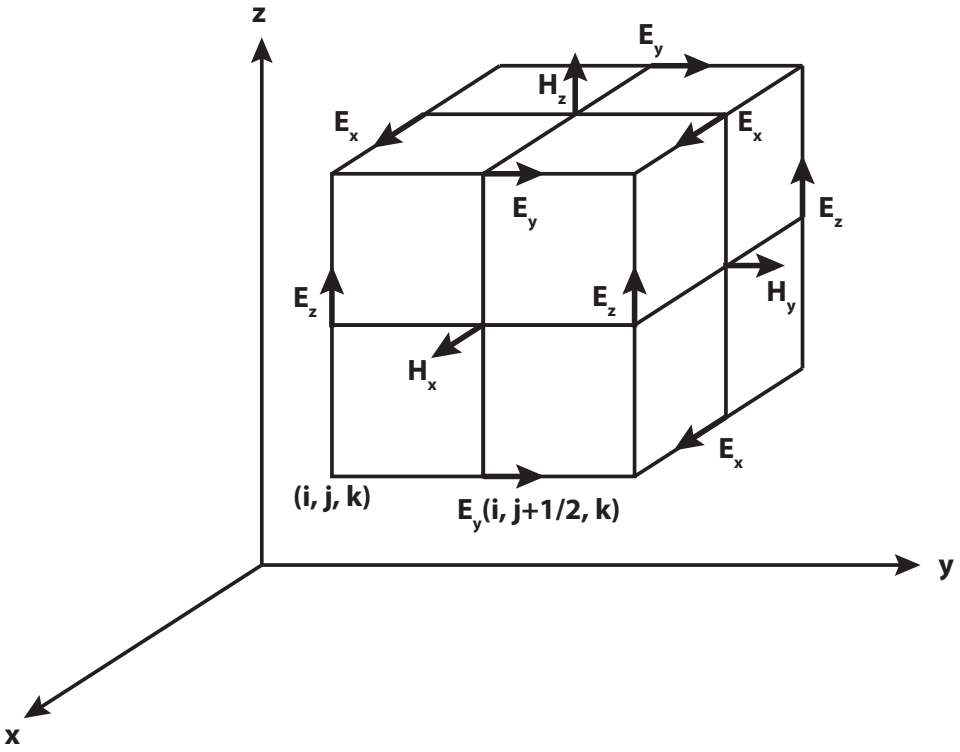

Figure 3.1: The uniform Yee FDTD grid wherein each $\vec{H}$ component is surrounded by four circulating $\vec{E}$ components, and each $\vec{E}$ component is surrounded by four circulating $\vec{H}$ components.

finite-difference expression for the temporal derivative occurs over over $\pm \Delta t/2$, which allows the resulting finite-difference equations to be implemented as a leapfrog algorithm wherein $\vec{E}$ and $\vec{H}$ are computed at alternating time steps.

Applying finite differences in Equations (3.10) to (3.15), taking into account the necessity for leapfrogging in time, produces the following set of difference equations:

$$\begin{aligned} E_{scat,\,x}\big|_{i+1/2,\,j,\,k}^{l+1} = {} & E_{scat,\,x}\big|_{i+1/2,\,j,\,k}^{l} + \\ & A\big|_{i+1/2,\,j,\,k}\,[H_{scat,\,z}\big|_{i+1/2,\,j+1/2,\,k}^{l+1/2} - H_{scat,\,z}\big|_{i+1/2,\,j-1/2,\,k}^{l+1/2} + \\ & \quad H_{scat,\,y}\big|_{i+1/2,\,j,\,k-1/2}^{l+1/2} - H_{scat,\,y}\big|_{i+1/2,\,j,\,k+1/2}^{l+1/2}] - \\ & \quad B\big|_{i+1/2,\,j,\,k}\ \frac{\partial E_{inc,\,x}}{\partial t}\bigg|_{i+1/2,\,j,\,k}^{l} \end{aligned} \tag{3.20}$$

$$\begin{aligned} E_{scat,\,y}\big|_{i,\,j+1/2,\,k}^{l+1} = {} & E_{scat,\,y}\big|_{i,\,j+1/2,\,k}^{l} + \\ & A\big|_{i,\,j+1/2,\,k}\,[H_{scat,\,x}\big|_{i,\,j+1/2,\,k+1/2}^{l+1/2} - H_{scat,\,x}\big|_{i,\,j+1/2,\,k-1/2}^{l+1/2} + \\ & \quad H_{scat,\,z}\big|_{i-1/2,\,j+1/2,\,k}^{l+1/2} - H_{scat,\,z}\big|_{i+1/2,\,j+1/2,\,k}^{l+1/2}] - \\ & \quad B\big|_{i,\,j+1/2,\,k}\ \frac{\partial E_{inc,\,y}}{\partial t}\bigg|_{i,\,j+1/2,\,k}^{l} \end{aligned} \tag{3.21}$$

$$\begin{aligned} E_{scat,\,z}\big|_{i,\,j,\,k+1/2}^{l+1} = {} & E_{scat,\,z}\big|_{i,\,j,\,k+1/2}^{l} + \\ & A\big|_{i,\,j,\,k+1/2}\,[H_{scat,\,y}\big|_{i+1/2,\,j,\,k+1/2}^{l+1/2} - H_{scat,\,y}\big|_{i-1/2,\,j,\,k+1/2}^{l+1/2} + \\ & \quad H_{scat,\,x}\big|_{i,\,j-1/2,\,k+1/2}^{l+1/2} - H_{scat,\,x}\big|_{i,\,j+1/2,\,k+1/2}^{l+1/2}] - \\ & \quad B\big|_{i,\,j,\,k+1/2}\ \frac{\partial E_{inc,\,z}}{\partial t}\bigg|_{i,\,j,\,k+1/2}^{l} \end{aligned} \tag{3.22}$$

$$H_{scat,\,x}\big|^{l+1/2}_{i,\,j+1/2,\,k+1/2} = H_{scat,\,x}\big|^{l-1/2}_{i,\,j+1/2,\,k+1/2} + \frac{\Delta t}{\mu_0 \Delta}[E_{scat,\,y}\big|^{l}_{i,\,j+1/2,\,k+1} - E_{scat,\,y}\big|^{l}_{i,\,j+1/2,\,k} + E_{scat,\,z}\big|^{l}_{i,\,j,\,k+1/2} - E_{scat,\,z}\big|^{l}_{i,\,j+1,\,k+1/2}] \tag{3.23}$$

$$H_{scat,\,y}\big|^{l+1/2}_{i+1/2,\,j,\,k+1/2} = H_{scat,\,y}\big|^{l-1/2}_{i+1/2,\,j,\,k+1/2} + \frac{\Delta t}{\mu_0 \Delta}[E_{scat,\,z}\big|^{l}_{i+1,\,j,\,k+1/2} - E_{scat,\,z}\big|^{l}_{i,\,j,\,k+1/2} + E_{scat,\,x}\big|^{l}_{i+1/2,\,j,\,k} - E_{scat,\,x}\big|^{l}_{i+1/2,\,j,\,k+1}] \tag{3.24}$$

$$H_{scat,\,z}\big|^{l+1/2}_{i+1/2,\,j+1/2,\,k} = H_{scat,\,z}\big|^{l-1/2}_{i+1/2,\,j+1/2,\,k} + \frac{\Delta t}{\mu_0 \Delta}[E_{scat,\,x}\big|^{l}_{i+1/2,\,j+1,\,k} - E_{scat,\,x}\big|^{l}_{i+1/2,\,j,\,k} + E_{scat,\,y}\big|^{l}_{i,\,j+1/2,\,k} - E_{scat,\,y}\big|^{l}_{i+1,\,j+1/2,\,k}] \tag{3.25}$$

where $A|_{i\,,j,\,k}$ and $B|_{i\,,j,\,k}$ are defined as

$$A|_{i\,,j,\,k} = \frac{\Delta t}{\epsilon|_{i,j,k} \cdot \Delta} \tag{3.26}$$

$$B|_{i,\,j,\,k} = \Delta t \left(1 - \frac{1}{\epsilon_r|_{i,j,k}}\right) \tag{3.27}$$

and the temporal derivatives of the incident field, $\vec{E}_{inc}$, are evaluated analytically. With the scattered fields known up to the previous time step, Eqs. (3.20) to (3.25) can be used to find the fields in the next time step over the entire grid.

3.3 Boundary conditions - perfectly matched layer

In order to perform the FDTD algorithm, it is necessary to terminate the edges of the computational domain with an appropriate boundary condition. For simulation of open-region scattering problems, a perfectly matched layer (PML) is a popular choice. The PML is an artificial layer of material that is formulated to ideally create no reflections regardless of frequency, polarization, or angle of incidence of a plane wave [16]. The PML, originally developed by Berenger [1], works by splitting each vector field component into two other orthogonal components. The 12 resultant components are then expressed in a coupled set of first-order partial differential equations. By choosing the loss parameters appropriately in these equations, a perfectly matched interface is derived. As an example, upon expanding the source-free Faraday's law (Equation (3.2)) into components, one of the resulting three equations is

$$\left(\mu\frac{\partial}{\partial t}+\sigma^*\right)H_x=\frac{\partial E_y}{\partial z}-\frac{\partial E_z}{\partial y}. \tag{3.28}$$

For the PML formulation, this equation is split into two equations:

$$\left(\mu\frac{\partial}{\partial t}+\sigma_y^*\right)H_{xy}=-\frac{\partial\left(E_{zx}+E_{zy}\right)}{\partial y} \tag{3.29}$$

$$\left(\mu\frac{\partial}{\partial t}+\sigma_z^*\right)H_{xz}=\frac{\partial\left(E_{yx}+E_{yz}\right)}{\partial z} \tag{3.30}$$

In the resulting equations, it is possible to specify the electric and magnetic conductivities of the PML in each direction; these are chosen to yield zero reflectivity for all angles of incidence of a wave [29]. In the discretized FDTD

grid, PML grid cells are placed in a thin shell around the computational domain. Since in FDTD there is discrete sampling of the governing equations, numerical artifacts due to finite spatial sampling will arise. To reduce reflection errors, the conductivities are graded to rise from zero in the PML shell region. For the code used in these simulations, the PML is set to be 20 grid cells thick, resulting in field reflections from the boundary of no more than -40dB [26].

3.4 Obtaining time-harmonic fields

The FDTD technique provides the instantaneous electromagnetic fields at each time step. For focused beam simulations, it is desirable to compute the time-harmonic fields from the instantaneous electromagnetic fields so that the beam intensity distributions may be computed and visualized. After the model has reached steady-state, phasor quantities can be computed using a running discrete Fourier transform (DFT) over subsequent FDTD time steps. Recursive DFT summation is performed at each grid point concurrent with FDTD time stepping because the recursive approach is memory efficient [29]. Summation over a full period is necessary because the DFT operates under the assumption that the signal is periodic. In practice, DFT summation over 50-100 optical periods, irrespective of exact summation over an integer multiple of optical periods, is sufficient to obtain nearly exact phasor quantities [17].

Assuming a single-mode laser beam in the simulations, $\vec{E}$ or $\vec{H}$ can be

written in the following form:

$$\vec{U}(\vec{r},t) = \tilde{\vec{U}}(\vec{r})e^{j\omega t} = |\vec{U}(\vec{r})|e^{j\phi(\vec{r})}e^{j\omega t} \tag{3.31}$$

The recursive calculation of the DFT is:

$$\widetilde{U}_{x,real}\Big|_{i,j,k}^{l} = \widetilde{U}_{x,real}\Big|_{i,j,k}^{l-1} + U_x\Big|_{i,j,k}^{l} \cdot \cos(\omega \cdot l\Delta t) \tag{3.32}$$

$$\widetilde{U}_{x,imag}\Big|_{i,j,k}^{l} = \widetilde{U}_{x,imag}\Big|_{i,j,k}^{l-1} + U_x\Big|_{i,j,k}^{l} \cdot \sin(\omega \cdot l\Delta t). \tag{3.33}$$

Here, U_x is a field component of $\vec{U}$, and $\widetilde{U}_x$ is the corresponding phasor. Equations (3.32) and (3.33) are used to obtain the magnitude and phase, respectively, of the phasor $\widetilde{U}_x$ for each node in the model grid:

$$\left|\widetilde{U}_x\right| = \sqrt{\widetilde{U}_{x,real}^2 + \widetilde{U}_{x,imag}^2} \tag{3.34}$$

$$\angle\widetilde{U}_x = \tan^{-1}\left(\frac{\widetilde{U}_{x,imag}}{\widetilde{U}_{x,real}}\right). \tag{3.35}$$

In practice, $\tilde{\vec{E}}(\vec{r})$ is computed, which is then used to calculate the optical intensity distribution, $I(\vec{r}) \propto \left|\tilde{\vec{E}}(\vec{r})\right|^2$.

Chapter 4

STED Microscopy Simulations

Using the previously derived beams and scattered-field FDTD algorithm, optical scattering of the STED excitation and de-excitation beams through biological cells is simulated. The goal of these simulations is to understand how the beams are scattered at depth, how the beam foci shift relative to one another, and how these effects alter the resulting fluorescence emission in terms of spot size and signal strength.

4.1 Geometry and properties

In the simulations, biological cells are modeled as a large number of ellipsoids of differing refractive indices distributed in 3D space. The various ellipsoids represent cellular components and organelles. This method of geometry creation was largely adapted from [26]. An example volume rendering of a single cell is shown in Figure 4.1. A summary of the properties used in the simulations is shown in Table 4.1. The background medium index of refraction is chosen to match that of cytoplasm, and the optically thin cell membrane is not included in the model. The nuclei and mitochondria are explicitly modeled. Other organelles are divided by volume into two groups:

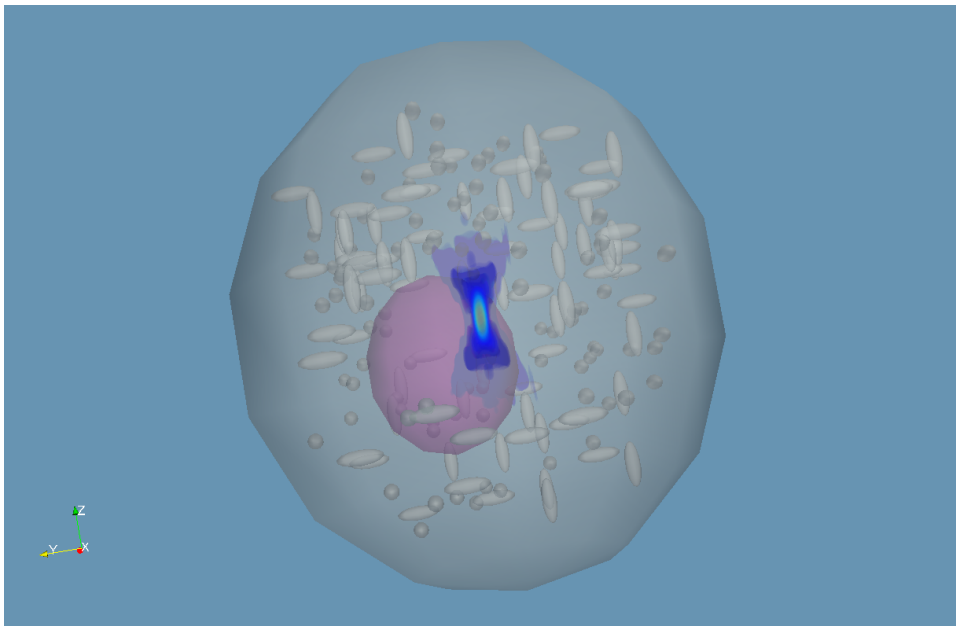

Figure 4.1: Volume rendering of a typical one cell geometry with the excitation beam intensity distribution overlaid. Nuclear inhomogeneities are not shown.

one group of larger ellipsoidal organelles and one group of smaller spherical organelles. Inhomogeneities are included within the nucleus to model the disordered distribution of nuclear proteins, which have been shown to enhance scattering [7]. The nuclear inhomogeneities consist of overlapping spheres of slightly varying refractive index placed randomly within the ellipsoidal nucleus region [27]. The spheres are randomly assigned refractive index values in the range $n_{min} \leq n \leq n_{max}$ and are drawn from a uniform distribution. In these simulations, $n_{min} = 1.4 - 0.03$ and $n_{max} = 1.4 + 0.03$, with 1.4 being the average refractive index of the nucleus.

4.2 Methods

A scattering geometry consisting of three stacked cells, each occupying roughly 13 x 13 x 15 μm is constructed. The optical properties and sizes of the cellular components are computed as described in Section 4.1. The optical axis is along the $+z$ direction, and the total extent of the model is 48 microns in depth. This geometry is depicted in Figure 4.2. A monochromatic beam at 770 nm is used to simulate excitation of the ATTO647N dye as described in [2]. While it would be more realistic to use a 635 nm wavelength beam for one-photon excitation of this dye (where one-photon absorption is appreciable), a 770 nm wavelength (the two-photon absorption peak) is used to simulate both one- and two-photon excitation. This simplification is made so that the resulting PSF dimensions for the one- and two-photon excitation cases of STED can be directly compared. The objective lens NA is set to 1.2.

Simulations are run for the excitation beam, the doughnut de-excitation beam, and the axial confinement de-excitation beam focused to 9 different depths relative to the location of the most superficial cell membrane. The simulated depths range from 1.8 μm, to 41.8 μm in 5 μm steps (see Figure 4.2). For each focus depth, a focused excitation beam of the form described previously is simulated as incident in the problem space. Once the FDTD model runs to steady state, the code calculates and saves the time-harmonic electric field data within a predetermined volume near the beam focus. A second simulation is run using the doughnut depletion beam nominally focused to the same point, and the volumetric field data is again recorded. Finally, a

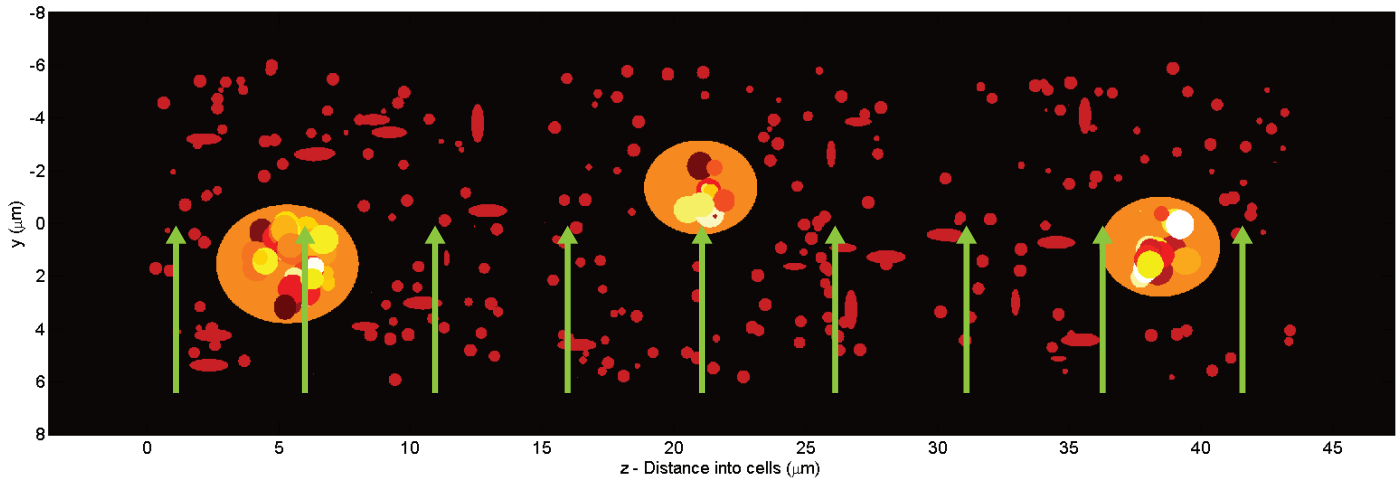

Figure 4.2: A YZ plane projection of the three cell geometry used in the simulations. Z is the optical axis, and the colors coorespond to different refractive indices. Green arrows indicate the nominal focus locations of the beams.

third simulation of the same variety is run using the axially-confined depletion beam. The beam intensity distribution is computed for the two depletion beams. These are analyzed independently to determine how the beam profiles are perturbed as the focal depth increases. The excitation and depletion fields are then analyzed together to determine the size of the resulting fluorescence volume and therefore the effective PSF of the STED imaging technique for given beam powers and focal depths.

For numerical stability and accuracy, the FDTD grid size is chosen to be $\Delta = \lambda_{min}/20$, where λ_{min} is the wavelength of the incident beam within the medium of largest refractive index in the model space. The model is run until the scattered field values reach steady state. For a plane wave source turned on at the model boundary at $t = 0$, this typically occurs within 3 to 4 times the duration required for the signal to propagate from one end of the model space to the other [28]. In the scattered field FDTD implementation, the time to reach steady state is reduced because the source is imposed throughout the model geometry at $t = 0$, rather than just at one boundary of the model space.

4.3 Analysis

4.3.1 Beam scattering analysis

In the absence of scattering, the de-excitation beam profiles should ideally achieve an intensity null centered about the excitation beam focus. Otherwise, increasing the de-excitation beam power will reduce the fluorescence signal via simulated emission from the excited fluorescence state. Further-

more, in the presence of scattering, it is desirable to know to what degree the intensity minima of the axial and lateral confinement beams are maintained as the depth of focus increases. Changes in the depletion beam profiles may alter the shape and symmetry of the resulting PSF. It is also useful to investigate the location of the intensity maximum of the excitation beam relative to the location of the intensity minimums of the de-excitation beams nominally focused to the same depth. This offers insights into whether scattering shifts the focus of the beams by similar spatial extents, which may also affect the PSF.

4.3.2 Point spread function analysis

Estimation of the PSF of the STED microscope requires a model of the functional dependence of the PSF on the relative excitation and de-excitation beam powers. A simple model for this dependence has been approximately derived in the absence of scattering [31] and has been generalized to account for arbitrary intensity distributions of the depletion beams [12]. With the excitation and de-excitation beam intensities known in the presence of scattering, this model may be used to obtain a more realistic representation of the fluorescence light generation near the focus.

A factor $\eta(\vec{r})$ is defined as the fraction of fluorescence detected at a location $\vec{r}$ after depletion by the de-excitation beam [31]. With the excitation and de-excitation beam pulses temporally separated, $\eta(\vec{r})$ can be estimated

as [8]:

$$\eta(\vec{r}) \approx \exp\left(-\ln(2) \cdot I_{STED}(\vec{r})/I_s\right) \tag{4.1}$$

where $I_{STED}(\vec{r})$ is the de-excitation beam intensity, and I_s is the effective saturation intensity of the fluorophore. I_s is defined as the de-excitation intensity at which the the probability of fluorescence by the dye is reduced to 1/2. In general, it is a function of the orientations of the fluorophores, their rotational behavior, and the wavelength, polarization, and temporal evolution of the light [8]. One may intuitively note that increasing I_{STED} relative to I_s should increase the microscope resolution but decrease the total fluorescence light detected by depopulating the excited state in the regions flanking the excitation beam focus. Because the de-excitation beam spatial distribution is unchanged by changes in the incident intensity, Equation 4.1 may be rewritten as [31]:

$$\eta(\vec{r}) \approx \exp\left(-\ln(2) \cdot \zeta \cdot I_{STED}(\vec{r})\right) \tag{4.2}$$

where

$$\zeta = \max[I_{STED}(\vec{r})]/I_s. \tag{4.3}$$

In the simulations, ζ is scaled to simulate varying levels of stimulated emission and therefore change the microscope resolution. Finally, the effective PSF $h_{eff}(\vec{r})$ is defined as the remaining focal region where fluorescence may occur [9]:

$$h_{eff}(\vec{r}) \propto I_{exc}(\vec{r}) \cdot \eta(\vec{r}) \tag{4.4}$$

where $I_{exc}(\vec{r})$ is the excitation beam intensity. It is important to mention that the PSF of the detection optics has been explicitly ignored in this definition.

Nevertheless, this expression is a model of the fluorescence signal generated by the STED microscope with or without the presence of scatterers. To extend the use of Equation 4.4 to two-photon excitation of the dye, $I_{exc}(\vec{r})$ is simply squared in the analysis.

This model for the PSF is used to explore the efficacy of axial and lateral confinement beams for STED. In addition, the PSF size and the resulting signal fluorescence strength for various depths of focus and depletion beam powers under both one- and two-photon excitation are investigated.

4.4 Simulation Results

4.4.1 Beam scattering

4.4.1.1 Doughtnut-shaped de-excitation beam

It is useful to examine the degree to which the shape and focus location for the excitation and de-excitation beams are perturbed as a function of focal depth. Figure 4.3 depicts the trend in the central minimum intensity for the doughnut de-excitation beam with depth. Figure 4.4 shows lateral profiles for the doughnut beams. All data sets have been normalized to the maximum intensity of the unscattered field. The intensity is plotted along a y-axis line containing the beam's central intensity minimum. Since the doughnut beam is theoretically of zero intensity along the optical axis, the z coordinate of the effective minimum is defined as the z coordinate where the doughnut intensity distribution takes on a maximum. The location of the effective minimum is considered to be the doughnut beam focal point. Note that in Figures 4.3 and

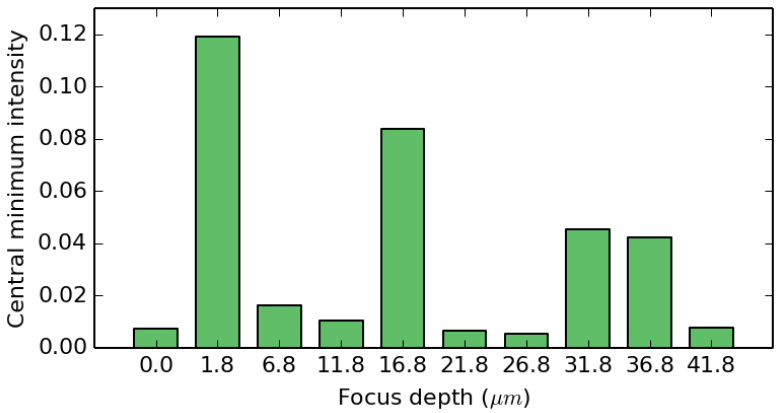

Figure 4.3: Intensity of the central minimum for the doughnut beam as a function of nominal focus depth. Note that a focus depth of zero cooresponds to the unscattered field.

4.4, the central minimum intensity is non-zero, even for the unscattered fields, because of discretization of the FDTD grid.

Figure 4.4 segments the intensity profiles into two groups: those for beams focused downstream of the cell nuclei (4.4a), and those for beams focused upstream of cell nuclei (4.4b). It is clear that the minimum intensities are largely unchanged for beams focused downstream of nuclei, but are perturbed by up to an order of magnitude for beams focused upstream of nuclei. In addition, the lateral location of the focus is more likely to measurably shift for the beams focused upstream of the nuclei. These results suggest that backscattering from nuclei is responsible for the perturbations and cause light from the doughnut ring to scatter into the minimum region. More generally, the backscattering effect causes a broadening of the intensity distribution adjacent to the doughnut region. This broadening of the de-excitation beam intensity

distribution will reduce the fluorescence signal ultimately emitted from the region. Despite the central minimum location and intensity perturbations, the overall shape of the the doughnut is largely maintained with increasing depth. This suggests that if excitation and de-excitation beams are co-aligned, sub-diffraction spot sizes should be achievable at even greater imaging depths than those modeled.

4.4.1.2 Axial confinement de-excitation beam

To assess the perturbations of the axial confinement beams with focus depth, the depth of the central axial minimum (Figure 4.5) and the beam profiles in the yz plane (Figure 4.6) are examined. The minimum location is defined as the central intensity minimum location along a z directed line containing the beam's intensity maximum. Note that for the unscattered beam, the depth of the central intensity minimum is 24% of the maximum intensity value. This fact highlights a serious limitation of the use of this beam for axial confinement: as the intensity of this beam is increased relative to the excitation beam, simulated emission will cause a reduction in the population of fluorophores that may contribute the to the useful fluorescence signal (at the beam focus). This limitation will be explored further in the context of the effective STED PSF.

4.4.1.3 Excitation beam

Figure 4.7 portrays the lateral profiles of the excitation beams, again grouped by the beam foci locations relative to the cell nuclei locations. Now the effective focal point is defined by the location of maximum intensity. The same trends are observed as for the doughnut beam: the overall intensity distribution broadens for positions upstream of nuclei where backscattering occurs. The lateral focus location is more likely to shift for these positions.

4.4.1.4 Beam shift quantification

In an effort to understand whether the shifts in the excitation and depletion beam foci tracked one another, the location of their foci were compared. Figure 4.8 portrays the effects of scattering on the beam foci locations. Figures 4.8a and 4.8b summarize the absolute shifts in focus location for each beam, while figure 4.8c quantifies the relative shift between beams. Figure 4.8c omits a comparison of the relative shift between beams in the z direction because the doughnut beam will be capable of successful lateral depletion over a large axial range. Clearly the relative lateral shifts are on the order of 50 nm at maximum across the simulated depths. Relative to the diffraction limited spot size, roughly 300 nm, this is a small shift, suggesting that STED should remain effective. However, the effect of a relative shift will be magnified as the depletion power is increased and will serve to reduce the fluorescence signal emitted compared to the unscattered case.

4.4.2 Point spread function

Using the intensity distributions for the excitation and de-excitation beams obtained from the scattering simulations, Equation 4.2 is used to calculate the fluorescence suppression and Equation 4.4 to compute the effective PSF of the STED microscope. The resulting size and magnitude of the fluorescence signal under both one- and two-photon excitation for varying de-excitation beam powers are considered.

Figure 4.9 demonstrates the process of PSF calculation in the absence of scattering. Rows 1, 2, and 3 depict the excitation, lateral confinement and axial confinement beam profiles used in the simulations. Row 4 depicts the resulting PSF using only the lateral confinement beam for STED, while row 5 depicts the resulting PSF using both the lateral and axial confinement beams at a 1:1 beam power ratio. The sub-diffraction limited size of the PSF is apparent by comparing it with the excitation beam size, which is diffraction-limited. When only the doughnut-shaped beam is used for depletion, the PSF contracts only in the radial dimension. When both de-excitation beams are used, both axial and lateral dimensions of the PSF become diffraction-unlimited.

It was previously noted that the axial confinement beam does not possess a null along the optical axis, even in the absence of scattering. Figure 4.10a shows an axial profile through a PSF computed using only the axial confinement beam. Figure 4.10b shows a lateral profile through a PSF using only the doughnut-shaped beam. The unscattered fields were used in both cases

to compute the PSF for purposes of demonstration. In both cases, the width of the fluorescence signal is reduced as the STED beam power is increased. However, for the case of axial confinement, the maximum fluorescence signal intensity drops with increasing de-excitation power, while with only lateral confinement it does not. While in principle this effect does not prevent imaging, in practice, imaging in highly scattering samples depends the detectability of the fluorescence emission. Also, given that the detected signal is related to the integrated intensity in the fluorescing volume, it is likely more desirable to sacrifice a fixed amount of signal in exchange for large lateral resolution gains compared to small gains in axial resolution. As a consequence, in the subsequent analysis of the effect of scattering on the PSF, the discussion is limited to de-excitation using the doughnut-shaped beam.

To understand the effect of scattering on PSF size, the PSF as a function of depth is computed for a number of different depletion beam powers (different values of ζ). The maximum intensity coordinates of the PSF are then located, the lateral profile along the y dimension is extrated, and the full-width at half maximum (FWHM) of the profile is computed. Figure 4.11a shows the resulting PSF widths for the case of one-photon excitation, while 4.11b shows the PSF widths for two-photon excitation. The maximum simulated ζ value is chosen to be 8 because, beyond this value, the PSF width approaches the FDTD grid size (22 nm), which may lead to inaccurate conclusions.

As expected, there is a consistent decrease in the FWHM as the deple-

tion power increases for both one- and two-photon excitation. The PSF width under two-photon excitation is smaller in the absence of any depletion beam power ($\zeta = 0$). This is a consequence of the simplifying assumption that the excitation wavelength for one- and two-photon excitation is identical. Because of the intensity-squared dependence of two-photon absorption, the lateral extent of the excitation beam profile is narrowed compared to the extent of the one-photon excitation profile. One may also observe that as the depletion power increases beyond the $\zeta = 4$ level, there is a rapidly diminishing return on the use of two-photon excitation. By this power level, saturated depletion by the doughnut-shaped beam largely overwhelms the gains obtained by using a spatially narrower excitation profile of two-photon excitation. This effect may be understood in terms of Equation 4.2: the STED beam profile does not change, but increasing the STED beam power through ζ exponentially decreases the possible fluorescence at a given location. The STED beam nominally has no intensity on the optical axis, so as ζ increases, the difference in PSF width for the one- and two-photon excitation cases should decrease. This does not, however, imply that there is no utility to using two-photon excitation with STED. As mentioned previously, two-photon imaging offers better localization of fluorescence excitation and the ability to detect signal photons that have been multiply scattered. These effects offer a distinct advantage for imaging of scattering samples over confocal detection.

There is little discernible trend in the PSF width as a function of depth. This is no surprise given that, as discussed previously, the central minimum

in the STED beam is largely retained as a function of depth, and central maxima and minima in the beams remain laterally co-aligned to within 44 nm over all simulated depths. Interestingly, the PSF width is elevated for the 16.8 nm focus depth, but only when the depletion power is non-zero. Referring to the corresponding STED beam profile in Figure 4.4a, one sees that the magnitude of the doughnut lobes at the 16.8nm depth are suppressed by roughly 50% relative to lobes in the unscattered case. Thus, less efficient depletion is expected, and therefore the PSF should be wider in this particular case.

Figures 4.12a and 4.12b show the integrated fluorescence signal in the lateral STED PSF for varying beam powers and focal depths under one-photon and two-photon excitation, respectively. This signal should be proportional to the signal detected using non-descanned detection in two-photon microscopy. Here the signal is used for general analysis. As expected, in both cases there is a downward trend in the fluorescence signal as ζ increases, implying that increasing depletion power results in less fluorescence emission from the excited region. However, there is little trend in the emission signal strength with depth. For the case of of no depletion beam power, this result can be understood by examining the excitation beam profiles (Figure 4.7). While there is evidence of lateral redistribution of intensity in each beam profile due to scattering, the overall magnitude of the integrated signal should not vary appreciably because the sidelobes contain little energy compared to the main lobe of the intensity profile. Upon application of depletion power for the one-photon case, the

signal as a function of depth changes shape compared to the unscattered case. The resulting trend is largely maintained as the depletion power increases. In the two-photon case, the trend in signal with depth is largely unchanged upon application of the depletion beam. As discussed previously, the normalized two-photon excitation profile is narrower than the single-photon excitation profile. By similar arguments to those discussed above, the depletion beam will immediately suppress fluorescence signal in the one-photon case whereas that excitation signal is inherently suppressed in the two-photon case. As the depletion power increases, the effect on the beam profile width, and thus the integrated emission signal lessens.

Cellular Component	Representation	Refractive Index	Major Diameter	Minor Diameter	% of Cell Volume
Background	N/A	$n = 1.36$	N/A	N/A	N/A
Cytoplasm	Ellipsoid	$n = 1.36$ [4]	15	13	N/A
Mitochondria	Ellipsoid	$n = 1.38$ [19]	3	1	4%
Nucleus	Ellipsoid	$n = 1.40$ [4]	6	5	18%
Nuclear Inhomogeneities	Spheres	$n = 1.4 \pm 0.03$	1	N/A	N/A
Organelles (Type 1)	Ellipsoid	$n = 1.38$	1.5	0.5	3%
Organelles (Type 2)	Sphere	$n = 1.38$	1	N/A	3%

Table 4.1: Cellular optical properties

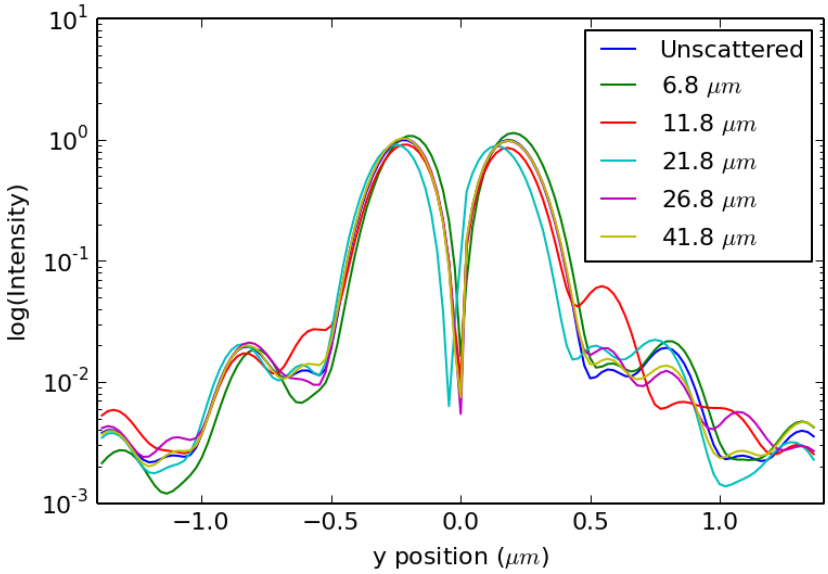

(a) Doughnut-shaped beams focused downstream of cell nulcei.

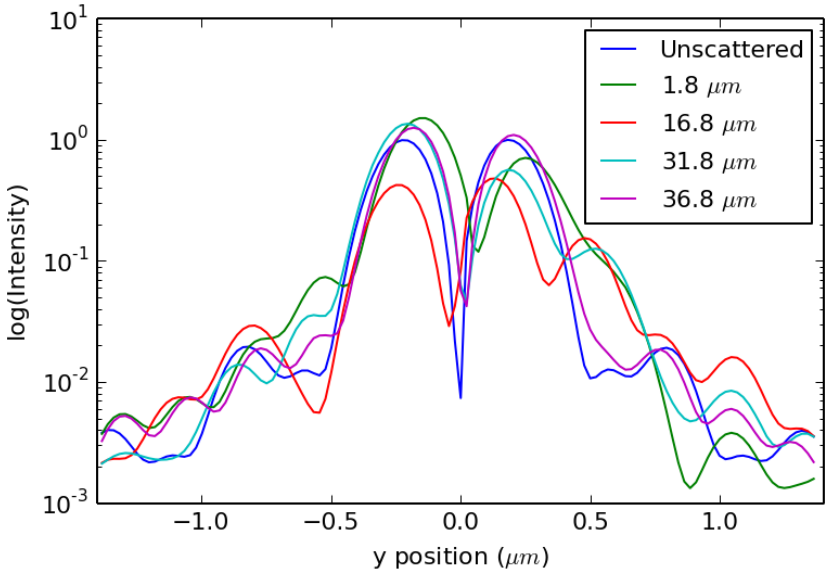

(b) Doughnut-shaped beams focused upstream of cell nulcei.

Figure 4.4: Lateral profiles of the doughnut de-excitation beams for varying focus depths at the effective focal plane.

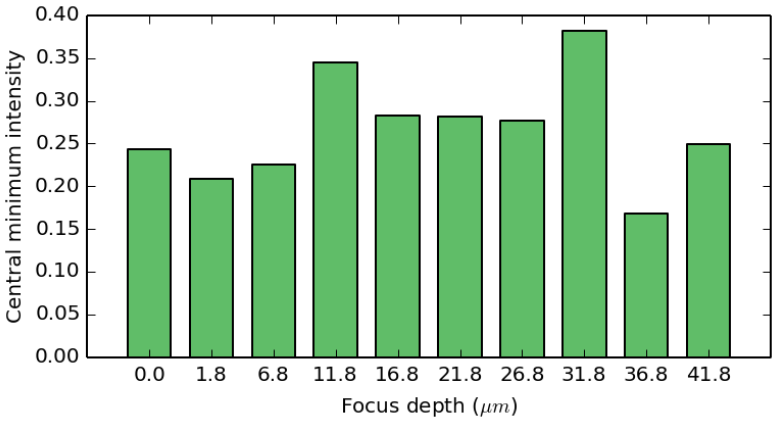

Figure 4.5: Intensity of the central minimum for the axial confinement beam as a function of nominal focus depth.

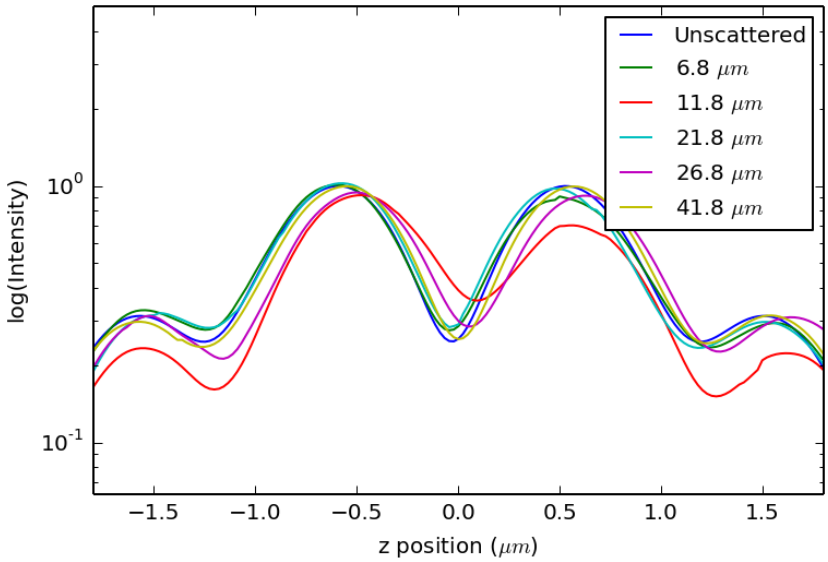

(a) Axial confinement beams focused downstream of cell nulcei.

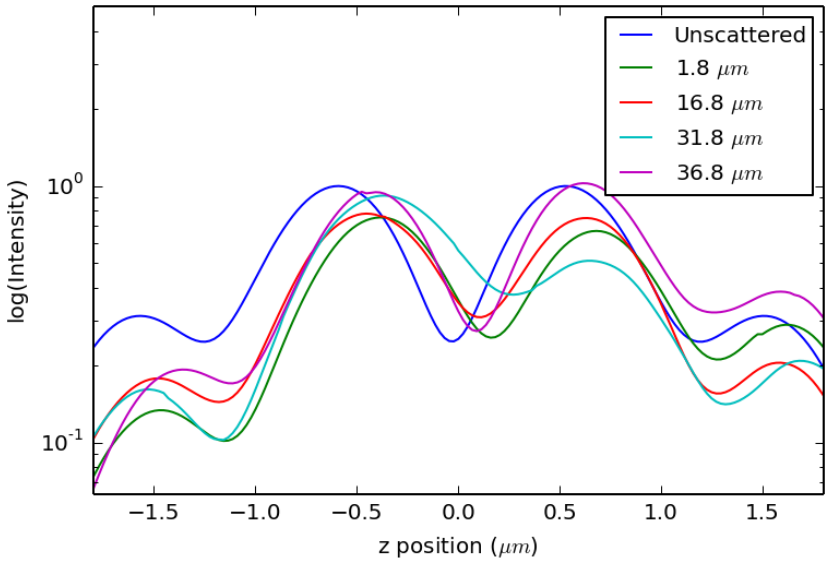

(b) Axial confinement beams focused upstream of cell nulcei.

Figure 4.6: Axial profiles of the axial confinement beams for varying focus depths at the effective focal plane. The z=0 location cooresponds to the nominal beam focus for a given focal depth.

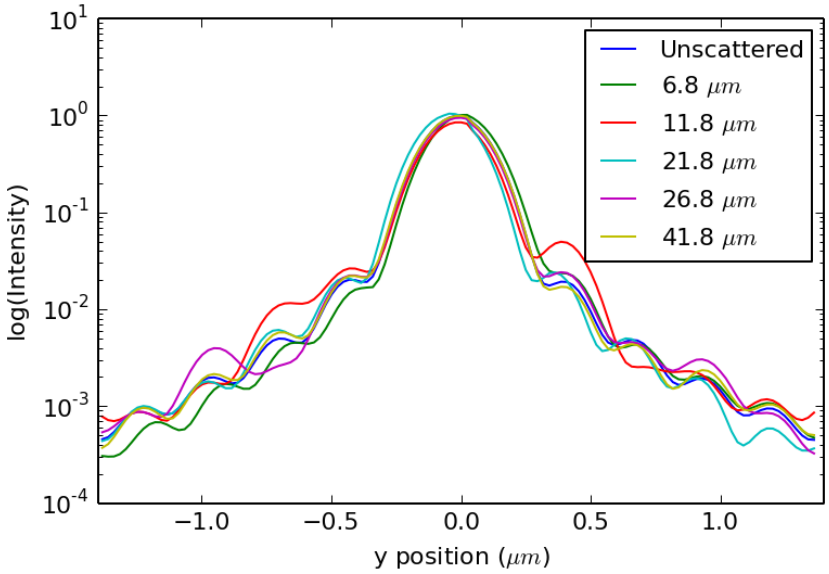

(a) Excitation beams focused downstream of cell nulcei.

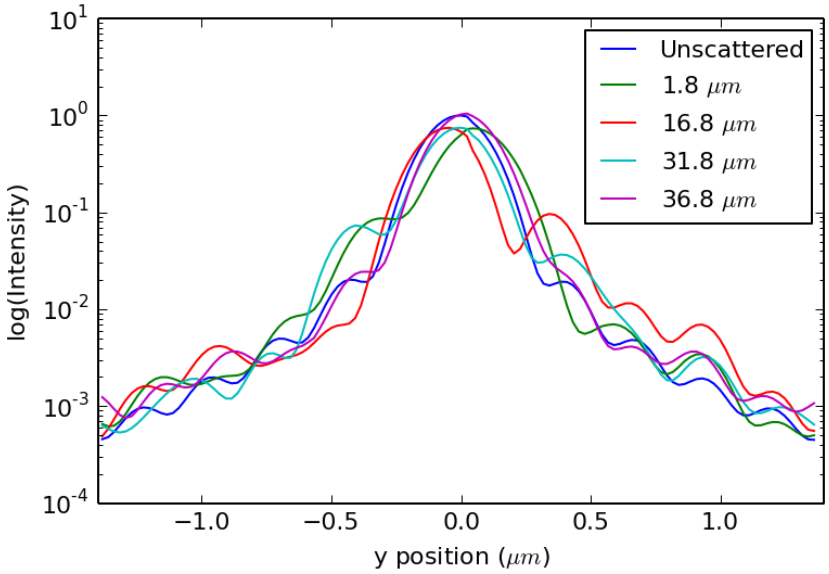

(b) Excitation beams focused upstream of cell nulcei.

Figure 4.7: Lateral profiles of the excitation beams for varying focus depths at the effective focal plane.

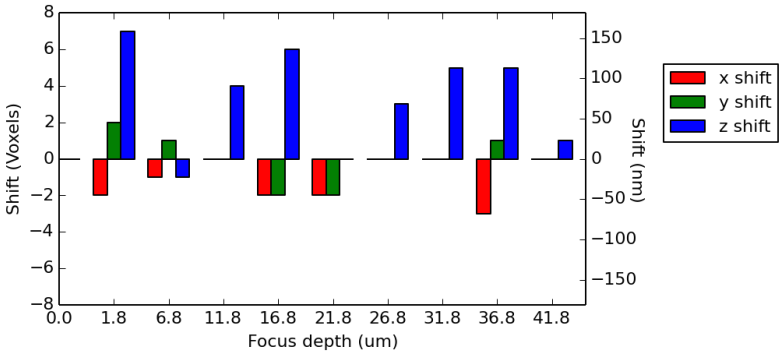

(a) Excitation beam - focus shift

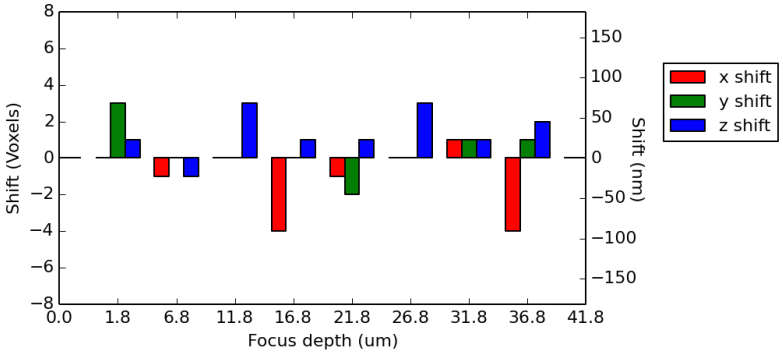

(b) Doughnut-shaped beam - focus shift

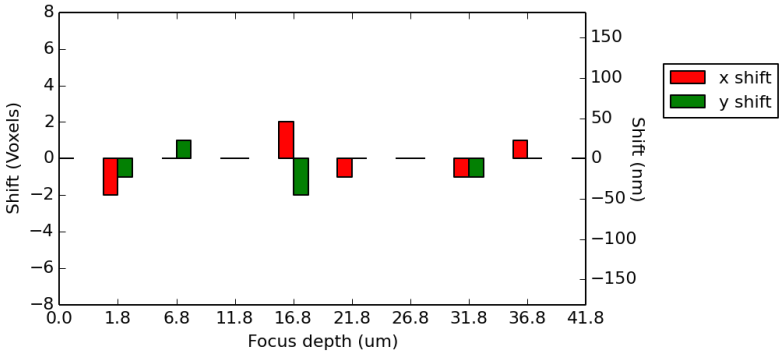

(c) Relative focus shift between beams

Figure 4.8: Shift in location from the nominal focus for the excitation and doughnut beams as a function of depth.

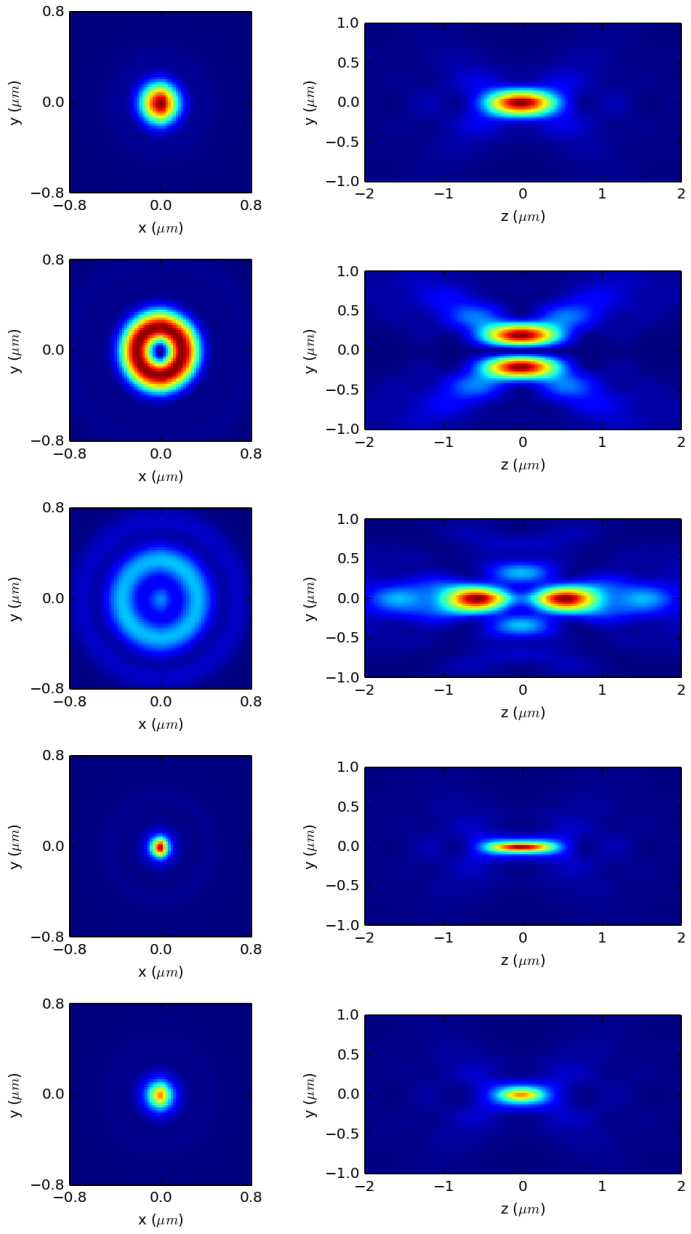

Figure 4.9: A demonstration of the PSF calculations in the absense of scattering for $\zeta = 3$. Row 4 - using only the lateral depletion beam. Row 5 - using both axial and lateral depletion beams at a 1:1 beam power ratio.

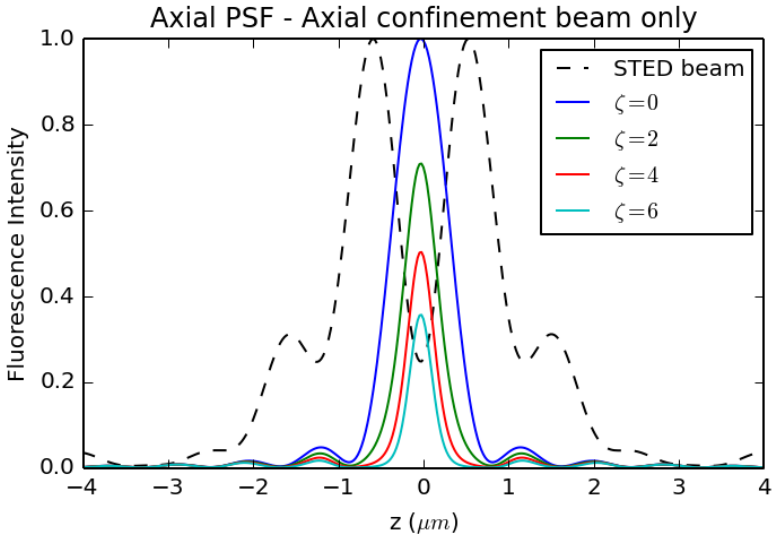

(a) Axial PSF using the axial confinement beam for de-excitation.

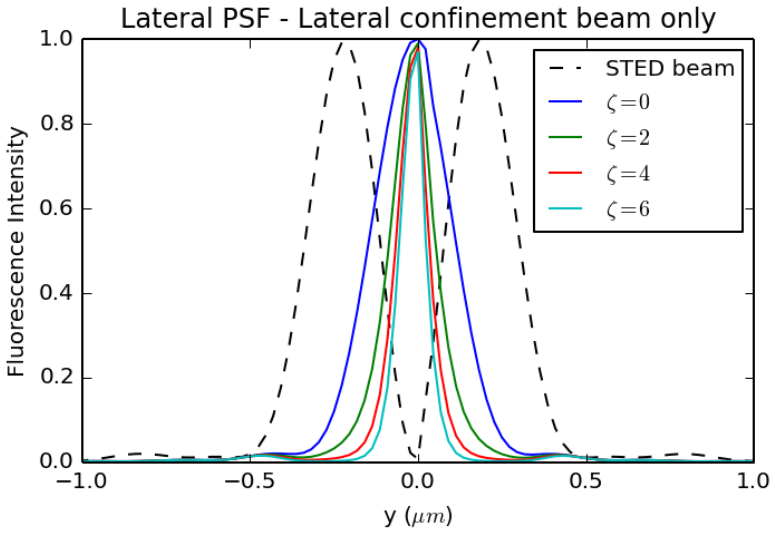

(b) Lateral PSF using the lateral confinement beam for de-excitation.

Figure 4.10: Demonstration of flouresence signal attenuation by the axial confinement beam, even in the absence of scattering.

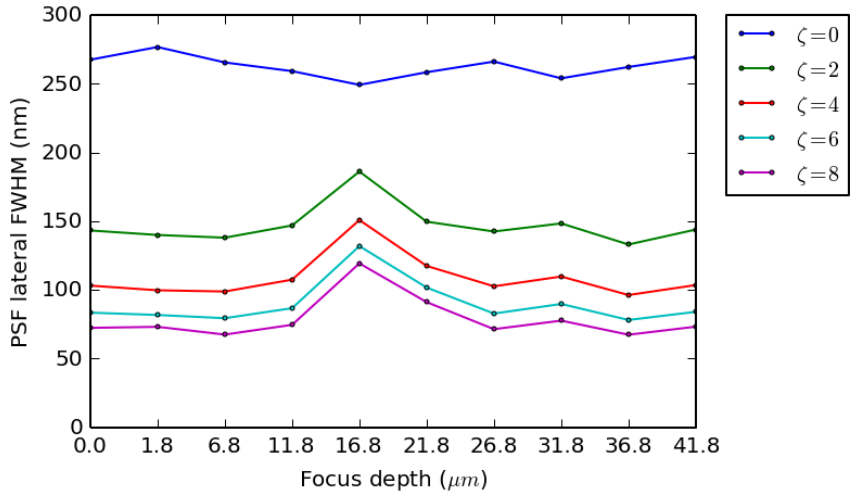

(a) One-photon excitation

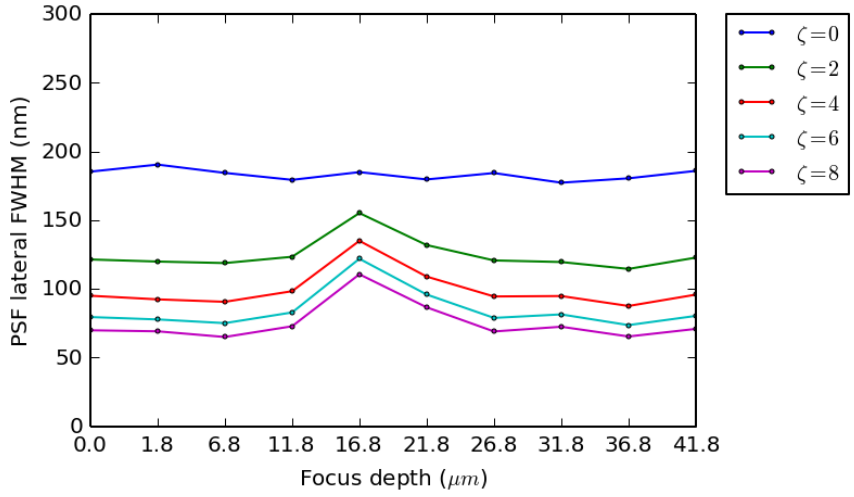

(b) Two-photon excitation

Figure 4.11: Lateral PSF width as a function of focal depth for varying depletion beam powers as set by ζ.

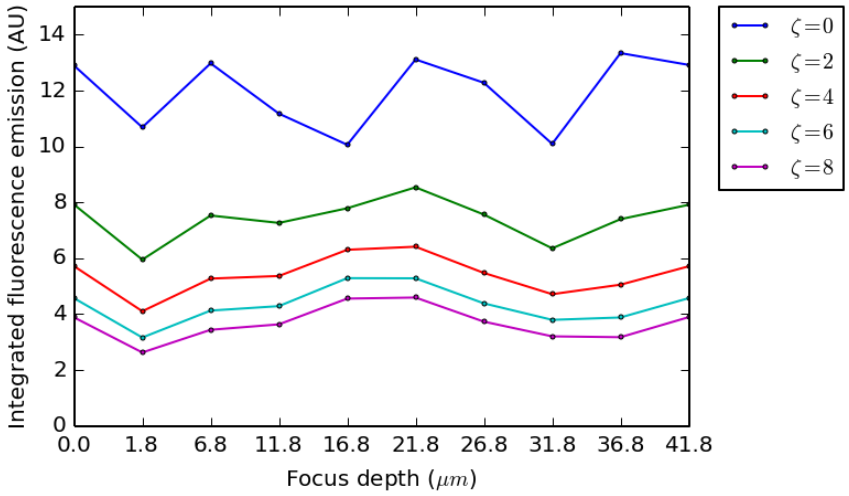

(a) One-photon excitation

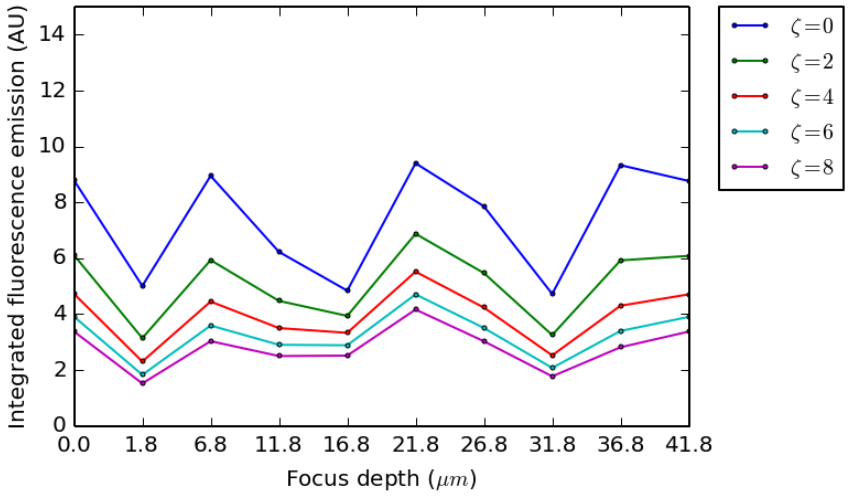

(b) Two-photon excitation

Figure 4.12: Integrated lateral fluorescence signal as a function of focal depth for varying depletion beam powers.

Chapter 5

Conclusions

5.1 Conclusions

The FDTD method was used to simulate optical scattering through biological cells under the illumination conditions used in STED microscopy. We derived the relevant beam models for the STED technique using a vectorial ray tracing approach and used these beams as the incident fields for the FDTD simulations. Furthermore, we described the scattered field implementation of the FDTD algorithm and presented a model for the fluorescence emission after STED.

These tools were used to analyze the effects of scattering on the excitation and de-excitation beam shapes and location of foci as a function of nominal focus depth. Results showed that the doughnut de-excitation beam maintains a well-defined intensity minimum as the depth of focus increases, though the intensity at the location of the minimum fluctuates as a function of depth. Furthermore a shift of focus location may occur, primarily because of the presence of heterogenous cell nuclei. Nevertheless, the relative shift between beams was shown to be minimal ($\leq$ 44 nm for any simulated depth).

Modeling of the STED microscopy PSF showed that the axial confine-

ment beam will inherently degrade the fluorescence signal strength due to the lack of a true intensity null, even in the absence of scattering. However, PSF calculations in the presence of cells using the lateral depletion beam revealed no appreciable decrease in PSF width or emission signal strength as a function of depth under both one- and two-photon excitation. This suggests that imaging at resolutions below the diffraction limit should remain possible as the depth of focus increases, so long as the fluorescence signal is practically detectable.

It was further seen that, as expected, two-photon excitation resulted in a fluorescence emission spot that was smaller than the one-photon emission spot at the same wavelength. However, as the depletion beam power increased, the spot widths under one- and two-photon excitation approached increasingly similar values.

Bibliography

[1] Jean-Pierre Berenger. Three-Dimensional Perfectly Matched Layer for the Absorption of Electromagnetic Waves. *Journal of Computational Physics*, 127(2):363–379, September 1996.

[2] Paolo Bianchini, Benjamin Harke, Silvia Galiani, Giuseppe Vicidomini, and Alberto Diaspro. Single-wavelength two-photon excitation-stimulated emission depletion (SW2PE-STED) superresolution imaging. *Proceedings of the National Academy of Sciences of the United States of America*, 109(17):6390–3, April 2012.

[3] Max Born and Emil Wolf. *Principles of Optics*. Cambridge University Press, 7 edition, 1999.

[4] A Brunsting and P F Mullaney. Differential light scattering from spherical mammalian cells. *Biophysical journal*, 14(6):439–53, June 1974.

[5] V E Centonze and J G White. Multiphoton excitation provides optical sections from deeper within scattering specimens than confocal imaging. *Biophysical journal*, 75(4):2015–24, October 1998.

[6] Jun B Ding, Kevin T Takasaki, and Bernardo L Sabatini. Supraresolution imaging in brain slices using stimulated-emission depletion two-photon laser scanning microscopy. *Neuron*, 63(4):429–37, August 2009.

[7] Andrew Dunn. *Light scattering properties of cells*. PhD thesis, The University of Texas at Austin, 1997.

[8] M Dyba, J Keller, and S W Hell. Phase filter enhanced STED-4Pi fluorescence microscopy: theory and experiment. *New Journal of Physics*, 7:134–134, May 2005.

[9] Marcus Dyba and Stefan Hell. Focal Spots of Size $\lambda/23$ Open Up Far-Field Florescence Microscopy at 33 nm Axial Resolution. *Physical Review Letters*, 88(16):163901, April 2002.

[10] Marcus Dyba and Stefan W. Hell. Photostability of a Fluorescent Marker Under Pulsed Excited-State Depletion through Stimulated Emission. *Applied Optics*, 42(25):5123, 2003.

[11] Matthew R. Foreman and Peter Török. Computational methods in vectorial imaging. *Journal of Modern Optics*, 58(5-6):339–364, March 2011.

[12] Benjamin Harke, Jan Keller, Chaitanya K Ullal, Volker Westphal, Andreas Schönle, and Stefan W Hell. Resolution scaling in STED microscopy. *Optics express*, 16(6):4154–62, March 2008.

[13] Benjamin Harke, Chaitanya K Ullal, Jan Keller, and Stefan W Hell. Three-dimensional nanoscopy of colloidal crystals. *Nano letters*, 8(5):1309–13, May 2008.

[14] Stefan W Hell. Microscopy and its focal switch. *Nature methods*, 6(1):24–32, January 2009.

[15] Fritjof Helmchen and Winfried Denk. Deep tissue two-photon microscopy. *Nature methods*, 2(12):932–40, December 2005.

[16] Jian-Min Jin. *Theory and Computation of Electromagnetic Fields*. Wiley-IEEE Press, 1 edition, 2010.

[17] SH Kim, SK Kim, and YH Lee. Vertical beaming of wavelength-scale photonic crystal resonators. *Physical Review B*, 73(23):235117, 2006.

[18] Thomas A Klar, Stefan Jakobs, Marcus Dyba, Alexander Egner, and Stefan W Hell. Fluorescence microscopy with diffraction resolution barrier broken by stimulated emission. *Proceedings of the National Academy of Sciences*, 97(15):8206–8210, July 2000.

[19] H Liu, B Beauvoit, M Kimura, and B Chance. Dependence of tissue optical properties on solute-induced changes in refractive index and osmolarity. *Journal of biomedical optics*, 1(2):200–11, April 1996.

[20] Gael Moneron and Stefan W. Hell. Two-photon excitation STED microscopy. *Optics Express*, 17(17):14567, August 2009.

[21] Tobias Müller, Christian Schumann, and Annette Kraegeloh. STED microscopy and its applications: new insights into cellular processes on the nanoscale. *Chemphyschem : a European journal of chemical physics and physical chemistry*, 13(8):1986–2000, June 2012.

[22] Lucas Novotny and Bert Hecht. *Principles of Nano-Optics*. Cambridge University Press, 2nd edition, 2012.

[23] James Pawley. *Handbook of Biological Confocal Microscopy*. Springer, 3 edition, 2010.

[24] B. Richards and E. Wolf. Electromagnetic Diffraction in Optical Systems. II. Structure of the Image Field in an Aplanatic System. *Proceedings of the Royal Society A: Mathematical, Physical and Engineering Sciences*, 253(1274):358–379, December 1959.

[25] Roman Schmidt, Christian a Wurm, Annedore Punge, Alexander Egner, Stefan Jakobs, and Stefan W Hell. Mitochondrial cristae revealed with focused light. *Nano letters*, 9(6):2508–10, June 2009.

[26] Matthew S Starosta. *Three-dimensional computation of light scattering by multiple biological cells*. PhD thesis, 2010.

[27] Matthew S. Starosta and Andrew K. Dunn. Three-Dimensional Computation of Focused Beam Propagation through Multiple Biological Cells. *Optics Express*, 17(15):12455, July 2009.

[28] A Taflove and ME Brodwin. Numerical solution of steady-state electromagnetic scattering problems using the time-dependent Maxwell's equations. *Microwave Theory and Techniques, ...*, 23(8):623–630, 1975.

[29] Allen Taflove and Susan Hagness. *Computational Electrodynamics: The Finite-Difference Time-Domain Method*. Artech House, 3 edition, 2005.

[30] Nicolai T Urban, Katrin I Willig, Stefan W Hell, and U Valentin Nägerl. STED nanoscopy of actin dynamics in synapses deep inside living brain slices. *Biophysical journal*, 101(5):1277–84, September 2011.

[31] Volker Westphal and Stefan Hell. Nanoscale Resolution in the Focal Plane of an Optical Microscope. *Physical Review Letters*, 94(14):143903, April 2005.

[32] D Wildanger, R Medda, L Kastrup, and S W Hell. A compact STED microscope providing 3D nanoscale resolution. *Journal of microscopy*, 236(1):35–43, October 2009.

[33] Emil Wolf. Electromagnetic Diffraction in Optical Systems. I. An Integral Representation of the Image Field. *Proceedings of the Royal Society of London. Series A, Mathematical and Physical Sciences*, 253(1274):349–357, 1959.

[34] Kane Yee. Numerical solution of initial boundary value problems involving maxwell's equations in isotropic media. *IEEE Transactions on Antennas and Propagation*, 14(3):302–307, May 1966.